Journal of The Electrochemical Society

Modeling the Effect of Low Pt loading Cathode Catalyst Layer in Polymer Electrolyte Fuel Cells: Part I. Model Formulation and Validation

Journal of The Electrochemical Society, 2021 **168** 124514

Modeling the Effect of Low Pt loading Cathode Catalyst Layer in Polymer Electrolyte Fuel Cells: Part I. Model Formulation and Validation

Arturo Sánchez-Ramos,[1] Jeff T. Gostick,[2] and Pablo A. García-Salaberri[1,z]

[1]*Department of Thermal and Fluids Engineering, Universidad Carlos III de Madrid, 28911 Leganés, Spain*
[2]*Department of Chemical Engineering, University of Waterloo, Waterloo, ON, N2L 3G1, Canada*

A model for the cathode catalyst layer (CL) is presented, which is validated with previous experimental data in terms of both performance and oxygen transport resistance. The model includes a 1D macroscopic description of proton, electron and oxygen transport across the CL thickness, which is locally coupled to a 1D microscopic model that describes oxygen transport toward Pt sites. Oxygen transport from the channel to the CL and ionic transport across the membrane are incorporated through integral boundary conditions. The model is complemented with data of effective transport and electrochemical properties extracted from multiple experimental works. The results show that the contribution of the thin ionomer film and Pt/ionomer interface increases with the inverse of the roughness factor. Whereas the contribution of the water film and the water/ionomer interface increases with the ratio between the geometric area and the surface area of active ionomer. Moreover, it is found that CLs diluted with bare carbon provide lower performance than non-diluted samples due to their lower electrochemical surface area and larger local oxygen transport resistance. Optimized design of non-diluted samples with a good distribution of the overall oxygen flux among Pt sites is critical to reduce mass transport losses at low Pt loading.

 [DOI: 10.1149/1945-7111/ac4456]

Manuscript submitted June 30, 2021; revised manuscript received November 22, 2021. Published December 30, 2021.

Supplementary material for this article is available online

List of symbols

A_{film}	surface area of ionomer per Pt site / m^2
A_{Pt}^{active}	active Pt surface area / m^2
ASR_{pem}	area-specific ionic resistance / $m^2\ S^{-1}$
a_e	specific ionomer surface area / m^{-1}
a_{ECSA}	electrochemical Pt surface area / $m^2_{Pt}\ kg^{-1}_{Pt}$
a_{Pt}^{active}	active specific Pt surface area / m^{-1}
C_{O_2}	oxygen molar concentration / mol m^{-3}
$D_{O_2,air}$	oxygen diffusivity in air / $m^2\ s^{-1}$
E_c	activation energy of oxygen reduction reaction / J mol^{-1}
E_r	reversible cell voltage / V
E_w	activation energy of O_2 permeation in liquid water / J mol^{-1}
F	Faraday's constant / C mol^{-1}
f_t	effective catalyst layer thickness / $m^3\ kg_c^{-1}$
I^{local}	local current density / A m^{-2}
I/C	ionomer-to-carbon weight ratio / —
$i_{o,c}$	exchange current density of oxygen reduction reaction / A m^{-2}_{Pt}
j_c	volumetric current density of oxygen reduction reaction / A m^{-3}
k	local mass transport coefficient / —
L_{Pt}	platinum loading / $kg_{Pt}\ m^{-2}$
M_{O_2}	molecular mass of oxygen / kg mol^{-1}
m	mass / kg
N_{O_2}	oxygen flux / mol $m^{-2}\ s^{-1}$
n	exponent / —
n_{Pt}	number of Pt nano-particles on Pt/C particle / —
p	pressure / Pa
R	universal gas constant / J $mol^{-1}\ K^{-1}$ or mass transport resistance / s m^{-1}
RH	relative humidity / —
r_f	roughness factor (ratio between active Pt surface area and geometric area) / —
r_p	CL characteristic pore radius / m
r_c	radius of carbon particles / m
s^{avg}	average water saturation in CL / —
T	temperature / K
T_{end}	simulated physical time / s
t_c	characteristic time / s
V	volume / m^3
V_{cell}	cell voltage / V
wt	Pt/C weight ratio / —
x	volume or number fraction / —
y	mass fraction / –

Greek letters

α_c	transfer coefficient of oxygen reduction reaction / –
β	ratio of volumetric current densities / –
Γ	dimensionless parameter in Eq. 19 / –
γ	reaction order of oxygen reduction reaction / –
δ	thickness / m
ε	porosity or volume fraction / –
η	overpotential / V
Θ_p	dimensionless parameter in Eq. 8 / –
θ_{PtO}	Pt-oxide coverage factor / –
Λ	parameter in Eq. 24 / A m^{-3}
ρ	density / kg m^{-3}
σ	conductivity / S m^{-1}
τ	tortuosity / –
Υ	dimensionless parameter in Eq. 19 / –
Φ_{macro}^{iso}	volume fraction of isolated macropores in CL / –
ϕ	potential / V
Ψ_w	permeability coefficient of oxygen in bulk liquid water / mol $m^{-1}\ Pa^{-1}\ s^{-1}$
ω	energy parameter of Temkin isotherm / J mol^{-1}

Subscripts

a	anode
bare	bare carbon

[z]E-mail: pagsalab@ing.uc3m.es

(Continued).

c	cathode or carbon
ch	channel
chcl	channel-CL
cl	catalyst layer
e	electrolyte (i.e., ionomer)
e^-	electric
film	ionomer thin film
geo	geometric
H^+	ionic
O_2	oxygen
Pt	platinum
Pt/C	Pt/C catalyst particle
p	pore
pw	pore/water interface
s	solid
w	water
we	water/ionomer interface
Superscripts	
avg	average
dif	diffusion
dry	dry conditions
eff	effective
eq	equivalent
in	inlet
knud	Knudsen
loc	local quantity
molec	molecular
ref	reference
sat	saturation
T	total
wet	wet conditions

Polymer electrolyte fuel cells (PEFCs) are promising power sources for future automotive vehicles due to several superior features, including zero emissions, low noise, rapid operation and high efficiency.[1–3] However, there are still critical issues related to the reduction of Pt loading, which have a significant effect on performance, durability and cost.[4–7] Improving the catalyst layer (CL) design is mandatory to mitigate mass transport losses caused by thin ionomer films, while ensuring a good ionic conductivity through the ionomer structure and the interfaces with the membrane (PEM).[8–11] Engineering of the pore structure,[12] wettability[13] and ionomer network[14] plays a critical role in the design of high performance, durable low Pt loading[15–17] and Pt-free[18,19] CLs.

In this context, an increasing number of works have been presented in the last years analyzing the properties, performance and durability of CLs. These contributions have provided relevant information on the main effective transport properties of CLs (effective diffusivity,[20–24] permeability,[25] and effective thermal,[26–28] electrical[29–31] and ionic[32–35] conductivities), as well as electrochemical properties, such as electrochemical surface area (ECSA) and exchange current density.[36–48] Nevertheless, further effort is still necessary to deconvolute the coupled phenomena that take place in CLs and optimize this key component. For example, there is a lack of fundamental knowledge on the multiscale ionomer structure of the CL, and the interplay between proton conduction, oxygen diffusion and water transport in low Pt loading CLs. This task is challenging due to the impossibility to visualize simultaneously the ionomer structure, Pt particles and water distribution within the nanometric CL geometry.[49,50] As a result, mathematical modeling and simulation currently provides valuable information while waiting for further experimental developments.[51–53] Relevant experimental and numerical works presented during the last decade on the matter are reviewed below.

Greszler et al. (2012)[54] examined the effect of cathode Pt loading (0.03–0.4 $mg_{Pt}\,cm^{-2}$) on oxygen transport resistance. The results showed that the electrode oxygen transport resistance was inversely proportional to Pt loading (i.e., Pt surface area), severely limiting the oxygen concentration at the Pt surface at low Pt loading. The "anomalous" resistance was equivalent to ~35 nm of a thin ionomer film covering Pt sites. Owejan et al. (2013)[55] studied the effect of Pt dispersion in CLs with different Pt/C weight ratios, while maintaining the Pt loading and electrode thickness constant by dilution with bare carbon. It was found that the local mass transport loss near Pt particles was not fully captured with the normalized Pt area. Additional geometric considerations, including the ionomer-to-Pt surface area ratio and interfacial resistances at both the gas and Pt interfaces of ionomer films, were necessary to explain the performance loss at low Pt loading. Spingler et al. (2017)[56] used a hydrogen-pump, limiting-current setup to examine gas-phase transport losses through CLs and various gas diffusion layers (GDLs) and micro-porous layers (MPLs). It was shown that the GDL effective diffusivity strongly depends on liquid saturation, even though the overall mass transport resistance was dominated by the CL, especially at low Pt loadings. The losses were separated into different mechanisms, including diffusion and mass-dependent and independent processes. The transport resistance of the ionomer film was found to be the main source of mass transport loss in the CL, while losses at the ionomer interfaces represented between 15% and 45% depending on the Pt loading. In a subsequent work, Schuler et al. (2019)[57] used the hydrogen-pump setup to study the effect of temperature, humidity and Pt/C weight ratio on the local oxygen transport resistance. It was confirmed that the CL resistance is composed of diffusion and interfacial components, the largest contribution being caused by Knudsen and ionomer diffusive resistance (~60%), followed by interfacial resistances at the ionomer interface (~20%) and molecular diffusive resistance (~20%). Recently, Salari et al. (2020)[58] investigated ex situ and in situ gas diffusivity in the CL, with a focus on the contribution of pores, ionomer and water to mass transfer. They found that the resistance of ionomer and water accounts for around 80% of the total resistance, and the rest is almost due to secondary pores. Primary pores had a notable impact on the oxygen relative diffusivity in ionomer and water, so that increasing their diameter linearly increased the oxygen diffusivity. A higher CL porosity raised the oxygen diffusivity in ionomer and water by a power of three.

Multiple modeling works have also been published in the literature dealing with transport phenomena and optimization of low Pt loading CLs, with a significant growth from 2019. Yoon and Weber (2011)[59] presented a model for the cathode CL, including the effect of Pt oxide, ionomer film resistance and non-linear reaction order. The results showed that increased oxygen diffusion pathways through ionomer films can substantially decrease performance due to higher diffusion resistance at low Pt loading. Hao et al. (2015)[60] developed a micro-scale model of the CL, which accounted for transport resistances of ionomer and water films and their interfaces. The CL model was incorporated into a 3D macroscopic model of a differential cell and results compared in good agreement with previous experimental data.[55] Moreover, they concluded that the effect of agglomerate size on cell performance is negligible for agglomerate radii lower than 150 nm, which is presumably the most common situation found in practice. Goshtasbi et al. (2019)[61] presented a 2D transient PEFC model, which accounted for a comprehensive description of the microstructure of the various cell layers. The model was used to examine the effect of cathode Pt loading on water transport. As the Pt loading (CL thickness) was reduced, they found that more water is transported toward the anode at low temperature since the resistance to water back diffusion is lowered, while this trend is reversed at high temperature due to increased volumetric heat generation with reduced thickness. Liu et al. (2019)[62,63] examined the dependency of effective transport properties on reaction rate, presenting a 1D upscaling method to

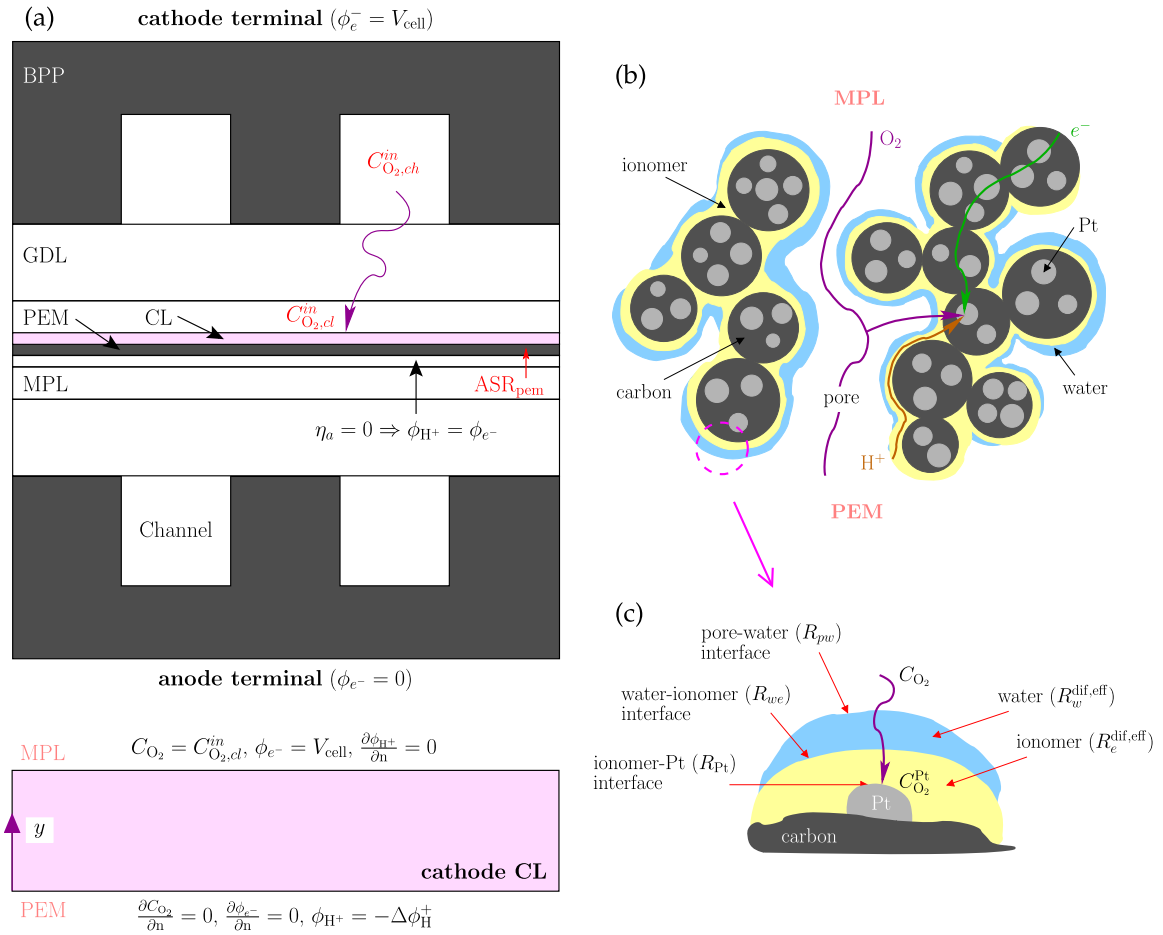

Figure 1. (a) Schematic of the location of the cathode CL in the MEA and the domain of the 1D model of the cathode CL, showing the local coordinate system y and the prescribed boundary conditions. The model also accounts for ohmic losses due to proton transport in the PEM and its interfaces through the area-specific ionic resistance, $\Delta\phi_{H^+} = I^{avg}ASR_{pem}$, as well as the oxygen concentration drop from the cathode channel, $C^{in}_{O_2,ch}$, to the MPL/CL interface, $C^{in}_{O_2,cl}$. Other losses are neglected. (b) Sketch of the internal microstructure of the CL, indicating the transport pathways of oxygen (through the pore space, and water and ionomer films), electrons (through carbon and Pt particles) and protons (through ionomer and water films). (c) Close-up view of the five oxygen transport resistances from the pore space to each active Pt nano-particle: (i) the interfacial resistance at the pore/water interface, R_{pw}, (ii) the diffusive resistance across the water film, $R_w^{dif,eff}$, (iii) the interfacial resistance at the water/ionomer interface, R_{we}, (iv) the diffusive resistance across the thin ionomer film, $R_e^{dif,eff}$, and (v) the interfacial resistance at the ionomer/Pt surface, R_{Pt}.

evaluate effective diffusivity and catalyst utilization of Pt-free CLs. The results showed that the effective diffusivity and catalyst utilization are affected by reaction-diffusion coupling when the Thiele modulus is higher than 1, an effect that can be important at high current densities in the cathode CL of state-of-the-art PEFCs. Gwak et al. (2020)[64] updated the micro-scale model previously developed by Hao et al.[60] for the CL to include the effect of Pt particle size. The CL model was coupled with a 3D PEFC macroscopic model to analyze the effect of microstructural parameters and operating conditions on low Pt loading CLs. The numerical results were in good agreement with experimental oxygen transport resistance data and highlighted the sensitivity of low Pt loading CLs to degradation. Zheng et al. (2020)[65] developed a 1D model of the cathode CL to examine the effect of non-uniform degradation of catalyst particles across the thickness. The results showed that gradient CLs are one of the most effective structures to improve both cell performance and durability. Larger Pt particles near the CL/membrane can remarkably mitigate the loss of ECSA and Pt mass, but accelerate the Pt dissolution near the GDL/MPL interface. Optimized distributions were obtained by simultaneously varying the particle size and Pt loading gradients.

In this work, the modeling approach presented by Hao et al. and co-workers,[60,64] considering a spherical shape of Pt/C particles, is reworked to account for local heterogeneities in the CL composition, as well as variations in transport and electrochemical properties. For a given (average) carbon particle radius, r_p, there are eight independent parameters in the model, namely: (i) the local Pt loading, $L_{Pt,i}$, (ii) Pt/C weight ratio, wt_i, (iii) ionomer volume fraction, $\varepsilon_{e,i}$, (iv) carbon volume fraction, $\varepsilon_{c,i}$, (v) ionomer transport coefficient, $k_{e,i}$, (vi) water saturation, s_i^{avg}, (vii) electrochemical surface area, $a_{ECSA,i}$, and (viii) reference exchange current density, $i^{ref}_{o,c,i}$. A simplified version of the formulation was implemented in a 1D macroscopic model of the cathode CL, including variations in the local composition due to the use of two Pt/C catalysts. This simplification allowed a direct comparison with the numerical data of Hao et al.,[60] where average compositional, transport and electrochemical properties were assumed for all regions inside a local representative CL volume (i.e., a single volume-average value was used for $R^{local}_{O_2}$). Future extensions of the model shall focus on the analysis of CL heterogeneitiesusing multidimensional models.[66–68]

The organization of the paper is as follows. In Section Mathematical Model , the model formulation is presented. In Section Effective Transport Properties and Physicochemical Parameters , the correlations and characteristic values of effective transport properties and physicochemical parameters are discussed. In Section Model Validation, the model is validated against the experimental data of Sun et al.[69] and Owejan et al.,[55] including both

CLs diluted and non-diluted with bare carbon. Finally, the concluding remarks are presented.

Mathematical Model

Three macroscopic conservation Eqs. are included in the model: (i) proton conservation, (ii) electron conservation, and (iii) oxygen mass conservation. In a first approximation, the solution of the energy and water conservation equations was omitted for simplicity.

Assumptions and computational domain.—The main simplifying assumptions of the model are:

- Steady state operation, isothermal conditions and ideal gases.
- Full gas humidification ($RH_a^{in} = RH_c^{in} = 100\%$).
- The PEM is perfectly impermeable to gaseous species and convective transport in the CL is negligible due to nanometric pore sizes.
- The oxygen concentration drop from the channel to the MPL/CL interface and the ohmic loss in other components different from the cathode CL are quantified by an overall mass transport resistance, $R_{O_2,chcl}$, and an overall area-specific ionic resistance, ASR_{pem}, respectively.
- The CL microstructure is macroscopically homogeneous across the thickness, with spherical Pt and carbon particles. Pt nanoparticles are uniformly distributed on the surface of the carbon support. Spherical Pt/C particles are covered by a uniform thin ionomer film, which is in turn surrounded by a uniform water film. The thickness of the ionomer and water films is uniform.
- Liquid saturation is homogenous across the CL, and is quantified by the average value s^{avg}.
- Diffusive and interfacial oxygen transport resistances caused by thin ionomer films are proportional to the permeation resistance of oxygen in bulk liquid water, the proportionality transport resistance constants being equal to k_i.

The left panel of Fig. 1 shows a cross-sectional view of a MEA, indicating the location of the cathode CL. The computational domain accounts for a 1D description of the cathode CL along the y-coordinate, including ohmic losses due to ionic transport in the PEM and its interfaces, as well as the drop of the oxygen concentration from the cathode channel to the MPL/CL interface. Voltage losses in other components are neglected, since they are typically small compared to the previous two losses.[56,60] Therefore, the electronic and ionic potentials are known at opposite boundaries of the cathode CL. At the cathode CL/MPL interface, the electronic potential is equal to the actual cell voltage of the cathode terminal ($\phi_{e^-} = V_{cell}$). In contrast, at the cathode CL/PEM interface, the ionic potential is equal to the reference voltage of the anode terminal ($\phi_{e^-} = 0$), considering a negligible overpotential in the anode CL, i.e., $\eta_a = \phi_{e^-} - \phi_{H^+} \simeq 0 \Rightarrow \phi_{H^+} \simeq 0$.

Macroscopic transport.—The charge conservation equation of protons is given by

$$\nabla\cdot(-\sigma_{H^+}^{eff}\nabla\phi_{H^+}) = -j_c \qquad [1]$$

where $\sigma_{H^+}^{eff}$ is the effective ionic conductivity, ϕ_{H^+} is the ionic potential, and j_c is the volumetric current density (the negative sign accounts for consumption, i.e., $j_c > 0$). According to Ohm's law, the protonic flux, $j_{H^+} = -\sigma_{H^+}\nabla\phi_{H^+}^{eff}$, is directed from high to low ionic potentials (i.e., from the PEM to the cathode CL, so that the ionic potential is negative in the cathode CL, $\phi_{H^+} \leqslant 0$).

Similarly, the charge conservation equation of electrons is given by

$$\nabla\cdot(\sigma_{e^-}^{eff}\nabla\phi_{e^-}) = -j_c \qquad [2]$$

where $\sigma_{e^-}^{eff}$ is the effective electrical conductivity and ϕ_{e^-} is the electronic potential. According to Ohm's law, the electronic flux,

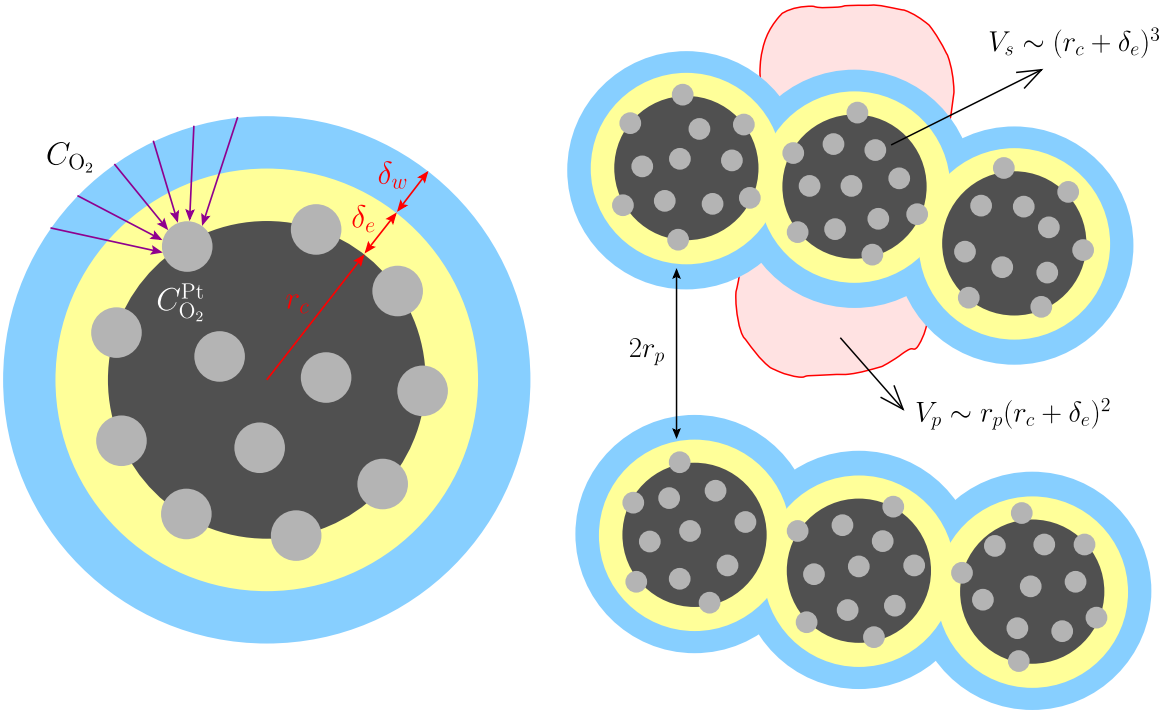

Figure 2. Schematic of the spherical geometry used to model the microstructure of the CL composed of Pt/C particles, surrounded by uniform thin ionomer and water films. The effective diffusion length across the ionomer and water films due to the sparse Pt particle distribution on Pt/C particles is illustrated on the left, while the estimation of the pore, V_p, and solid, V_s, volumes of the CL microstructure are shown on the right (see Supplementary Material (available online at stacks.iop.org/JES/168/124514/mmedia) for further details).

$\boldsymbol{j}_{e^-} = \sigma_{e^-}^{\text{eff}} \nabla \phi_{e^-}$, is directed from low to high electronic potentials (i.e., from the MPL to the cathode CL, so that the electronic potential is positive in the cathode CL, $\phi_{e^-} \geqslant V_{\text{cell}}$).

The mass conservation equation of oxygen is given by

$$\nabla \cdot (-D_{O_2}^{\text{eff}} \nabla C_{O_2}) = -\frac{j_c}{4F} \quad [3]$$

where $-j_c/4F$ is the volumetric consumption rate of oxygen according to Faraday's law, and $D_{O_2,\text{air}}^{\text{eff}}$ is the effective diffusivity of oxygen in air under wet conditions ($s^{\text{avg}} > 0$)

$$D_{O_2,\text{air}}^{\text{eff,wet}} = D_{O_2,\text{air}}^{\text{molec}} \underbrace{\frac{D_{O_2,\text{air}}^{\text{eff,dry}}}{D_{O_2,\text{air}}^{\text{molec}}}}_{f(\varepsilon_{cl})} \underbrace{\frac{D_{O_2,\text{air}}^{\text{eff,wet}}}{D_{O_2,\text{air}}^{\text{eff,dry}}}}_{g(s^{\text{avg}})} \quad [4]$$

In this expression, $D_{O_2,\text{air}}^{\text{molec}}$ is the molecular diffusivity of oxygen in air, $f(\varepsilon_{cl})$ is the normalized dry effective diffusivity, which accounts for the blockage of the unsaturated CL on gas diffusion, and $g(s^{\text{avg}})$ is the relative effective diffusivity, which accounts for the relative blockage of water saturation on gas diffusion. The molecular diffusivity depends on temperature, T, and gas-phase pressure, p_g, as follows[70]

$$D_{O_2,\text{air}}^{\text{molec}} = 2.65 \times 10^{-5} \left(\frac{T}{333}\right)^{1.5} \left(\frac{10^5}{p_{g,c}}\right) \quad [\text{m}^2\,\text{s}^{-1}] \quad [5]$$

where T is expressed in K and $p_{g,c}$ is expressed in Pa (the bulk diffusivity with pure oxygen feed is assumed approximately equal). The normalized dry effective diffusivity, $f(\varepsilon_{cl})$, is affected by the porosity of the CL, ε_{cl}, and the torusoity, τ, of transport pathways. In addition, Knudsen diffusion in the CL is important due to collision of molecules with walls in small primary (6–20 nm) and secondary (20–100 nm) pores.[71] As a result, $f(\varepsilon_{cl})$ can be expressed as[24]

$$f(\varepsilon_{cl}) = \frac{\varepsilon_{cl}}{\tau} \left(1 + \frac{D^{\text{molec}}}{D^{\text{knud}}}\right)^{-1} \quad [6]$$

where $D_{O_2}^{\text{knud}}$ is the Knudsen diffusivity

$$D_{O_2}^{\text{knud}} = \frac{2 r_p}{3} \left(\frac{8RT}{\pi M_{O_2}}\right)^{1/2} \quad [7]$$

Here, M_{O_2} is the molar mass of oxygen and r_p is the characteristic pore radius of the CL, which depends on porosity, ε_{cl}, radius of carbon particles, r_c, and thin ionomer film thickness, δ_e. As shown in Fig. 2, considering that the pore volume, $V_p \sim r_p (r_c + \delta_e)^2$, and the solid volume, $V_s \sim (r_c + \delta_e)^3$, the following expression is obtained for r_p

$$\varepsilon_{cl} = \frac{V_p}{V_{cl}} = \frac{1}{1 + \frac{V_s}{V_p}} \Rightarrow$$
$$r_p = \frac{1}{\Theta_p} \left(\frac{\varepsilon_{cl}}{1 - \varepsilon_{cl}}\right) (r_c + \delta_e) \quad [8]$$

where V_{cl} is the total CL volume and Θ_p is a dimensionless parameter of order unity, which accounts for the exact quantitative relationship between V_p and V_s (i.e., $V_p = \Theta_p V_s$). Here, $\Theta_p = 1$ was considered in a first approximation.

Volumetric current density.—The volumetric current density of the oxygen reduction reaction (ORR) can be expressed as[60]

$$j_c = i_{o,c}\, a_{\text{Pt}}^{\text{active}} (1 - \theta_{\text{PtO}}) \left(\frac{C_{O_2}^{\text{Pt}}}{C_{O_2}^{\text{ref}}}\right)^{\gamma} \times \exp\left(-\frac{\alpha_c}{RT} F \eta_c - \frac{\omega \theta_{\text{PtO}}}{RT}\right) \quad [9]$$

where $i_{o,c}$ is the exchange current density, ω is the energy parameter of the Temkin isotherm, γ is the reaction order, $C_{O_2}^{\text{Pt}}$ and $C_{O_2}^{\text{ref}}$ are the oxygen concentrations at the ionomer/Pt interface and reference conditions, respectively, $a_{\text{Pt}}^{\text{active}}$ is the active specific surface area, and $\eta_c = \phi_{e^-} - \phi_{H^+} - E_r$ is the cathode overpotential, with the reversible cell voltage, E_r, given by Ref. 72

$$E_r = 1.23 - 0.9 \times 10^{-3} (T - 298.15) + \frac{RT}{2F} \left[\ln(p_{H_2}^{in}) + \frac{1}{2} \ln(p_{O_2}^{in})\right] \quad [10]$$

In this expression, $p_{H_2,ch}^{in}$ and $p_{O_2,ch}^{in}$ are the inlet hydrogen and oxygen partial pressures (in atm)

$$p_{H_2} = p_{g,a}^{in} - \text{RH}_a p_{H_2O}^{\text{sat}};$$
$$p_{O_2} = 0.21 (p_{g,c}^{in} - \text{RH}_c p_{H_2O}^{\text{sat}}) \quad [11]$$

Table I. Transport and physicochemical parameters with a constant value.

Parameter	Symbol	Value	References
Density of carbon	ρ_c	1.95 g cm^{-3}	60, 64
Density of platinum (Pt)	ρ_{Pt}	21.45 g cm^{-3}	60, 64
Density of electrolyte (ionomer)	ρ_e	1.9 g cm^{-3}	60, 64
Radius of carbon particles	r_c	25 nm	60, 64
Pore-solid volume ratio parameter	Θ_p	1	Assumed
Transfer coefficient of ORR	α_c	0.5	60, 64
Reaction order of ORR	γ	0.7	60, 64
Ref. exchange current density of ORR	$i_{o,c}^{\text{ref}}$	3×10^{-5} A cm$_{\text{Pt}}^{-2}$	41–44, 46
Activation energy of ORR	E_c	67 kJ mol^{-1}	60, 64
Ref. O_2 concentration	$C_{O_2}^{\text{ref}}$	40 mol m^{-3}	60, 64
Energy parameter of Temkin isotherm	ω	3 kJ mol^{-1}	60
Ref. permeability coefficient of O_2 in bulk liquid water	Ψ_w^{ref}	3×10^{-13} mol m^{-1} s^{-1} Pa^{-1}	73
Act. energy of O_2 permeation in water	E_w	5 kJ mol^{-1}	73
Average water saturation in CL	s^{avg}	0.4	74

and $p_{H_2O}^{sat}$ is the saturation pressure of water, which is a strong function of temperature[61,66]

$$\log_{10}(p_{H_2O}^{sat}) = -2.18 + 2.95 \times 10^{-2}(T - 273.15) - 9.18 \times 10^{-5}(T - 273.15)^2 + 1.44 \times 10^{-7}(T - 273.15)^3 \quad [\text{atm}] \qquad [12]$$

The dependence of the exchange current density on temperature can be well correlated by the expression[60]

$$i_{o,c} = i_{o,c}^{ref} \exp\left[-\frac{E_c}{R}\left(\frac{1}{T} - \frac{1}{353.15}\right)\right] \qquad [13]$$

where $i_{o,c}^{ref}$ and E_c are the reference exchange current density and activation energy of ORR, respectively (see Table I).

The active Pt and ionomer specific surface areas, a_{Pt} and a_e, are related to the Pt loading, L_{Pt}, and ECSA, a_{ECSA}, as follows

$$a_{Pt}^{active} = \frac{A_{Pt,cl}^{active}}{V_{cl}} = \frac{A_{Pt,cl}^{active}}{m_{Pt,cl}} \frac{m_{Pt,cl}}{V_{cl}} = a_{ECSA} \frac{L_{Pt}}{\delta_{cl}} \qquad [14a]$$

$$a_e = \frac{A_e}{V_{Pt/C}} = \frac{4\pi(r_c + \delta_e)^2}{\frac{4}{3}\pi r_c^3 \varepsilon_c^{-1}} = 3\frac{\varepsilon_c}{r_c^3}(r_c + \delta_e)^2 \qquad [14b]$$

where $A_{Pt,cl}^{active}$ and $m_{Pt,cl}$ are the total active Pt surface area and mass of Pt in the CL, A_e and $V_{Pt/C}$ are the active ionomer surface area and the CL volume corresponding to a Pt/C particle, respectively, and ε_c is the carbon volume fraction.

According to Subramanian et al.,[75] the Pt-oxide coverage factor, θ_{PtO}, decreases exponentially with decreasing cathode potential, V_{cell}. A good correlation is provided by the following expression[60]

$$\theta_{PtO} = \frac{1}{1 + \exp[22.4(0.818 - V_{cell})]} \qquad [15]$$

Microstructural thicknesses and volume fractions.—The (average) thicknesses of the ionomer and water films can be expressed as a function of the radius of carbon particles, r_c, volume fractions of the CL constituents, ε_{cl}, ε_e, ε_c, and average liquid saturation, s^{avg}, through the following expressions

$$\frac{V_c + V_e}{V_c} = 1 + \frac{\varepsilon_e}{\varepsilon_c} = \frac{(r_c + \delta_e)^3}{r_c^3} \Rightarrow \delta_e = \left[\left(1 + \frac{\varepsilon_e}{\varepsilon_c}\right)^{1/3} - 1\right] r_c \qquad [16a]$$

$$\frac{V_c + V_e + V_w}{V_c} = 1 + \frac{\varepsilon_e}{\varepsilon_c} + \frac{\varepsilon_{cl} s^{avg}}{\varepsilon_c} = \frac{(r_c + \delta_e + \delta_w)^3}{r_c^3} \Rightarrow \delta_w = \left[\left(1 + \frac{\varepsilon_e}{\varepsilon_c} + \frac{s^{avg}\varepsilon_{cl}}{\varepsilon_c}\right)^{1/3} - 1\right] r_c - \delta_e \qquad [16b]$$

where the volume fractions of carbon, ionomer and pore (i.e., porosity) phases are equal to

$$\varepsilon_c = \frac{V_{c,cl}}{V_{cl}} = \frac{V_{c,cl}}{m_{Pt,cl}} \frac{m_{Pt,cl}}{V_{cl}} = \frac{1}{\rho_c}\left(\frac{1 - wt}{wt}\right)\frac{L_{Pt}}{\delta_{cl}} \qquad [17a]$$

$$\varepsilon_{Pt} = \frac{V_{Pt,cl}}{V_{cl}} = \frac{V_{Pt,cl}}{m_{Pt,cl}} \frac{m_{Pt,cl}}{V_{cl}} = \frac{1}{\rho_{Pt}} \frac{L_{Pt}}{\delta_{cl}} \qquad [17b]$$

$$\varepsilon_{e,cl} = \frac{V_{e,cl}}{V_{cl}} = \frac{m_{e,cl}}{m_{c,cl}} \frac{(m_{c,cl}/V_{c,cl})}{(m_{e,cl}/V_{e,cl})} \frac{V_{c,cl}}{V_{cl}} = \left(\frac{I}{C}\right)\frac{\rho_c}{\rho_e}\varepsilon_c \qquad [17c]$$

$$\varepsilon_{cl} = \frac{V_{p,cl}}{V_{cl}} = 1 - \frac{V_{c,cl} + V_{Pt,cl} + V_{e,cl}}{V_{cl}} = 1 - \varepsilon_c - \varepsilon_{Pt} - \varepsilon_e \qquad [17d]$$

Here, ρ_{Pt} and ρ_e are the densities of Pt and ionomer, respectively, $wt = m_{Pt,cl}/(m_{c,cl} + m_{Pt,cl})$ is the Pt/C weight ratio (i.e., the Pt mass fraction of the Pt/C catalyst) and $I/C = m_{e,cl}/m_{c,cl}$ is the ionomer-to-carbon weight ratio.

Local oxygen transport.—The oxygen concentration at active Pt sites in Eq. 9, $C_{O_2}^{Pt}$, is significantly lower than the oxygen concentration in the pore space, C_{O_2}, due to the local mass transport resistance toward each Pt site (including oxygen dissolution), $R_{O_2}^{local}(y)$, caused by water and ionomer films and their interfaces. A detailed derivation of the local mass transport resistance is available in Supplementary Material (available online at stacks.iop.org/JES/168/124514/mmedia). $C_{O_2}^{Pt}$ is determined by equating the local oxygen flux, $N_{O_2}^{local}(y)$, to the local oxygen consumption rate of the ORR, $I^{local}(y)/4F$, expressed per unit of geometric area

$$N_{O_2}^{local}(y) = \frac{C_{O_2}(y) - C_{O_2}^{Pt}(y)}{R_{O_2}^{local}(y)} = \frac{I^{local}(y)}{4F} \qquad [18]$$

where $I^{local}(y) = j_c(y)\delta_{cl} \geqslant 0$ is the local current density (per unit of geometric area).

$R_{O_2}^{local}$ can be decomposed into four terms: (i) the sum of the interfacial resistance at the pore/water interface and the diffusive resistance across the water film that covers the ionomer surface, $R_w = R_{pw} + R_w^{dif}$; (ii) the interfacial resistance at the water/ionomer interface, R_{we}; (iii) the diffusive resistance across the thin ionomer film, R_e^{dif}; and (iv) the interfacial resistance at the ionomer/Pt interface, R_{Pt}. The resulting expression for $R_{O_2}^{local}$ when the CL is composed of a single Pt/C catalyst (and possibly some bare carbon for dilution) is given by

$$R_{O_2}^{local}(y) = \left[\underbrace{\frac{\rho_c r_c^3}{3(r_c + \delta_e)^2}}_{\Upsilon\rho_c r_c}(\Gamma R_w + R_{we}) + \frac{1}{a_{ECSA}(1 - \theta_{PtO}(y))}\left(\frac{1 - wt}{wt}\right)(R_e + R_{Pt})\right]\frac{f_t}{\delta_{cl} x} \qquad [19]$$

where $\Gamma = (r_c + \delta_e + \delta_w)^2/(r_c + \delta_e)^2$ and $\Upsilon = r_c^2/[3(r_c + \delta_e)^2]$, x is the number or volume fraction of platinized carbon particles, and $f_t = (\rho_c \varepsilon_c)^{-1} = \delta_{cl} L_c^{-1}$ is the effective electrode thickness, with L_c the carbon loading.

Noting that $L_{Pt} = x(\delta_{cl}/f_t)[wt/(1 - wt)]$, Eq. 19 can be re-written as

$$R_{O_2}^{local} = \left[\Upsilon\rho_c r_c\left(\frac{wt}{1 - wt}\right)a_{ECSA}(\Gamma R_w + R_{we}) + \frac{1}{1 - \theta_{PtO}}(R_e + R_{Pt})\right] r_f^{-1} \qquad [20]$$

where $r_f^{-1} = (a_{ECSA} L_{Pt})^{-1}$ is the inverse of the roughness factor.

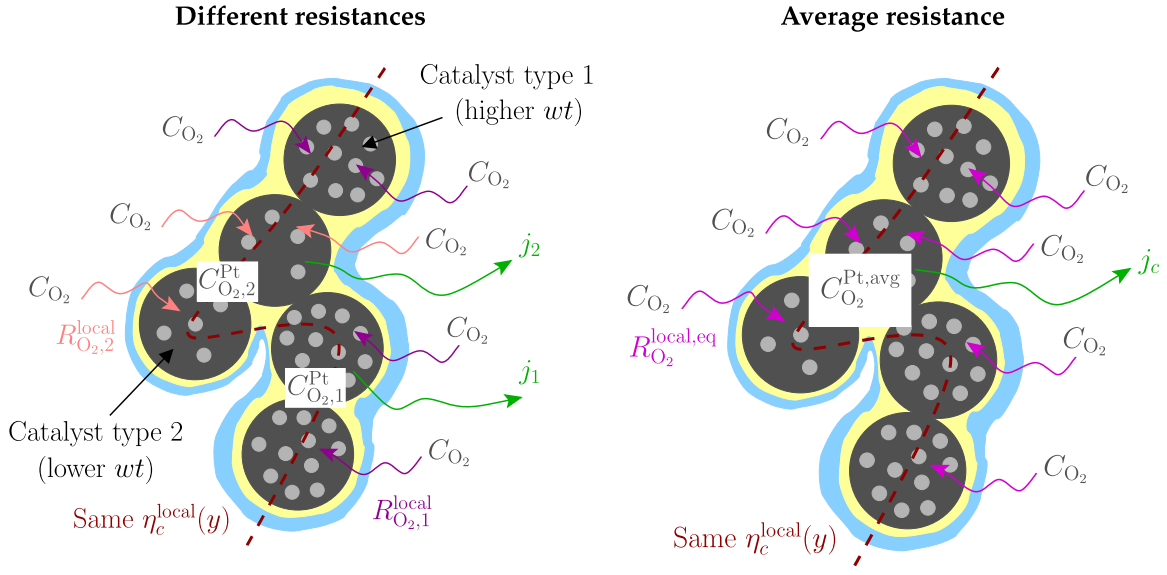

Figure 3. Schematic of the modeling approach used to model the local oxygen transport resistance, $R_{O_2}^{local}$, in variably loaded CLs with two different Pt/C weight ratios, wt_i ($i = 1, 2$): (left) present work with a local transport resistance for each Pt/C catalyst and (right) Hao et al.'s model[60] with a single volume-average local transport resistance for both Pt/C catalysts.

In the above expression, each local mass transport resistance is assumed to be proportional to the local resistance (per unit length) due to permeation (i.e., dissolution and diffusion) of oxygen in bulk liquid water, i.e., R_w, R_e, R_{we}, $R_{Pt} \propto R_w^{bulk} = (\Psi_w RT)^{-1}$, in order to have a common well-known reference. The expressions of the resistances are as follows

$$R_w = \frac{k_w \delta_w}{\Psi_w RT} = k_w \delta_w \frac{1}{\Psi_w RT} = k_w \delta_w R_w^{bulk} \quad [21a]$$

$$R_e = \frac{k_e \delta_e}{\Psi_w RT} = \left(\frac{k_e}{k_w}\right)\left(\frac{\delta_e}{\delta_w}\right) R_w = k_e \delta_e R_w^{bulk} \quad [21b]$$

$$R_{we} = \frac{k_{we} k_e \delta_e}{\Psi_w RT} = k_{we} R_e = k_{we} k_e \delta_e R_w^{bulk} \quad [21c]$$

$$R_{Pt} = \frac{k_{Pt} k_e \delta_e}{\Psi_w RT} = k_{Pt} R_e = k_{Pt} k_e \delta_e R_w^{bulk} \quad [21d]$$

where Ψ_w is the permeability coefficient of oxygen in bulk liquid water (i.e., in a non-constrained environment with infinitely fast dissolution kinetics), and k_w, k_e, k_{we} and k_{Pt} are dimensionless transport coefficients that account for the actual resistance of water and ionomer films and their interfaces.

Equation 20 is also valid for variably loaded CLs with two Pt/C catalysts, $i = 1, 2$, (and bare carbon)

$$R_{O_2,i}^{local} = \left[\Upsilon \rho_c r_c \left(\frac{wt_i}{1 - wt_i}\right) a_{ECSA} (\Gamma R_w + R_{we}) + \frac{1}{1 - \theta_{PtO}} (R_e + R_{Pt})\right] r_{f,i}^{-1} \quad [22]$$

where wt_i is the Pt/C weight ratio of catalyst i.

Using Eq. 18 for each Pt/C catalyst, we can write

$$N_{O_2,i}^{local}(y) = \frac{C_{O_2}(y) - C_{O_2,i}^{Pt}(y)}{R_{O_2,i}^{local}(y)} = \frac{j_{c,i}(y)\delta_{cl}}{4F} \quad [23]$$

And introducing the expression for $j_{c,i}(y)$, Eq. 9 with $a_{Pt,i}^{active}$ and $C_{O_2,i}^{Pt}(y)$, in the above equation, we yield

$$\Lambda_i(y)[C_{O_2,i}^{Pt}(y)]^\gamma - \frac{4F}{\delta_{cl} R_{O_2,i}^{local}} \times [C_{O_2}(y) - C_{O_2,i}^{Pt}(y)] = 0; \quad i = 1, 2 \quad [24]$$

where

$$\Lambda_i(y) = i_{o,c}\, a_{Pt,i}^{active} (1 - \theta_{PtO}) \left(\frac{1}{C_{O_2}^{ref}}\right)^\gamma \times \exp\left(-\frac{\alpha_c F}{RT}\eta_c(y) - \frac{\omega \theta_{PtO}}{RT}\right) \quad [25]$$

with

$$a_{Pt,i}^{active} = \frac{a_{ECSA} L_{Pt,i}}{\delta_{cl}}; \quad L_{Pt,i} = x_i \frac{\delta_{cl}}{f_t}\left(\frac{wt_i}{1 - wt_i}\right) \quad [26]$$

When $\gamma \neq 1$, the algebraic Eq. 24 must solved numerically for each Pt/C catalyst using a root-finding method to determine the local value of $C_{O_2,i}^{Pt}(y)$. Then, the local volumetric current density of each Pt/C catalyst, $j_{c,i}(y)$, can be evaluated with Eq. 9, and the local volumetric current density of the two Pt/C catalysts obtained as $j_c(y) = j_{c,1}(y) + j_{c,2}(y)$ (the corresponding local current density is given by $I^{local}(y) = \delta_{cl} j_c(y)$). In the case of a single Pt/C catalyst, only one algebraic equation has to be solved, since there is only one value of $C_{O_2}^{Pt}(y)$ and $j_c(y)$.

The present formulation for variably loaded CLs is different from that of Hao et al.[60] As shown in Fig. 3, the model in Ref. 60 considers the volume-average concentration at the active Pt surface, $C_{O_2}^{Pt,avg}$, instead of a different oxygen concentration for each Pt/C catalyst, $C_{O_2,i}^{Pt}$. As a result, an average local mass transport resistance, which depends on wt^{avg}, is used in Ref. 60 to couple local oxygen transport and electrochemical kinetics. The differences in terms of performance between both modeling approaches were found to be

small because the equivalent resistance, $R_{O_2}^{local,eq}$, in the present formulation is virtually equal to resistors in parallel (see Supplementary Material (available online at stacks.iop.org/JES/168/124514/mmedia)). Consequently, the oxygen flux is concentrated in the Pt/C catalyst with the minimum transport resistance or evenly distributed between both catalysts when their resistances are similar. In Hao et al.'s model,[60] these two situations correspond to y_1, $x_1 \ll y_2$, x_2 and y_1, $x_1 \approx y_2$, x_2, respectively. Nevertheless, significant differences in the local oxygen concentrations inside local representative CL volumes can arise due to other heterogeneities, such as variations of ε_e and/or k_e. For instance, previous experimental works have shown a significant difference in the performance at low Pt loading due to microstructural heterogeneities.[16,57,76–78]

Global outputs.—For a given cell voltage, V_{cell}, the average current density, I^{avg}, and equivalent local oxygen transport resistance, $R_{O_2,cl}^{local,eq}$, can be determined by averaging the local current density, I^{local}, and equivalent local oxygen transport resistance, $R_{O_2,cl}^{local,eq}$, across the CL thickness

$$I^{avg} = \frac{1}{\delta_{cl}} \int_0^{\delta_{cl}} I^{local}(y)\mathrm{d}y \qquad [27a]$$

$$R_{O_2,cl}^{local,eq} = \frac{1}{\delta_{cl}} \int_0^{\delta_{cl}} R_{O_2}^{local,eq}(y)\mathrm{d}y \qquad [27b]$$

where $R_{O_2}^{local,eq}$ is equal to the local oxygen resistance for a single Pt/C catalyst, $R_{O_2}^{local,eq} = R_{O_2}^{local}$, and approximately equal to resistors in parallel for variably loaded Pt/C catalysts

$$\frac{1}{R_{O_2}^{local,eq}} = \left[\frac{1}{R_{O_2,1}^{local}} + \frac{1}{R_{O_2,2}^{local}}\right]^{-1} \qquad [28]$$

The total oxygen transport resistance from the channel to each active Pt site is given by

$$R_{O_2}^{T} = R_{O_2,chcl} + R_{O_2,cl} + R_{O_2}^{local,\,eq} \Rightarrow$$
$$R_{O_2}^{T} = \frac{C_{O_2,ch}^{in} - C_{O_2}^{Pt}}{N_{O_2}^{avg}}; \quad N_{O_2}^{avg} = \frac{I^{avg}}{4F} \qquad [29]$$

where $R_{O_2,chcl}$ and $R_{O_2,cl}$ are the mass transport resistances (per unit of geometric area) from the channel to the MPL/CL interface (i.e., CL inlet) and across the CL bulk space, $R_{O_2,cl} = \delta_{cl}/D_{O_2,air}^{eff}$, respectively. As described in the next section, $R_{O_2,chcl}$ is introduced in the model with an integral boundary condition.

Boundary conditions.—Equations 1–3 are supplemented with the following boundary conditions at the CL/MPL and CL/PEM interfaces

$$C_{O_2} \Rightarrow \text{ CL/MPL: } C_{O_2} = C_{O_2,cl}^{in}; \quad \text{CL/PEM: } \frac{\partial C_{O_2}}{\partial \mathbf{n}} = 0 \qquad [30a]$$

$$\phi_{e^-} \Rightarrow \text{ CL/MPL: } \phi_{e^-} = V_{cell}; \quad \text{CL/PEM: } \frac{\partial \phi_{e^-}}{\partial \mathbf{n}} = 0 \qquad [30b]$$

$$\phi_{H^+} \Rightarrow \text{ CL/MPL: } \frac{\partial \phi_{H^+}}{\partial \mathbf{n}} = 0; \quad \text{CL/PEM: } \phi_{H^+} = -\Delta\phi_{H^+} \qquad [30c]$$

where V_{cell} is the operating cell voltage, $C_{O_2}^{in}$ is the inlet oxygen concentration at the MPL/CL interface, and $\Delta\phi_{H^+}$ is the drop of the ionic potential across the membrane (and its interfaces).

The last two quantities are related to the average current density, I^{avg}, through the following expressions

$$C_{O_2,cl}^{in} = C_{O_2,ch}^{in} - R_{O_2,chcl}\frac{I^{avg}}{4F} \qquad [31a]$$

$$\Delta\phi_{H^+} = ASR_{pem} I^{avg} \qquad [31b]$$

where $C_{O_2,ch}^{in}$ is the inlet oxygen concentration into the cell and ASR_{pem} is the area-specific ionic resistance of the membrane (and its interfaces).

Numerical implementation.—The system of three conservation Eqs. 1–3, subject to boundary conditions 30a–30c, was solved in Matlab using the built-in solver *pdepe* for 1D elliptic PDEs. A small value was prescribed for the pre-factor of the transient term ($c = 10^{-6}$ SI) to decrease the physical time to reach the steady-state solution, since transient dynamics were not of interest. The simulated physical time was set equal to $T_{end} = 1$ s, much higher than the characteristic times of the governing equations, $t_c \lesssim 10^{-12}$ s. Transient simulations shall be considered in future work to analyze, e.g., degradation.

The algebraic Eq. 24, which couples the macroscopic and microscopic sub-models, was solved with the bisection method inside the *pdepe* solver. This root-finding method was preferred over

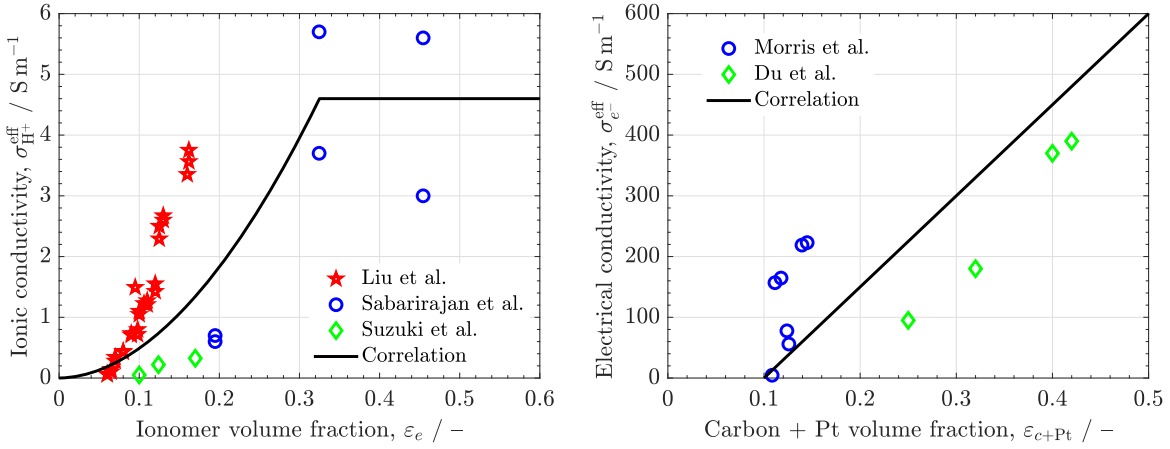

Figure 4. (Left) Variation of the effective ionic conductivity, $\sigma_{H^+}^{eff}$, as a function of the ionomer volume fraction, ε_e (Eq. 32), along with the experimental data of Liu et al.,[79] Sabarirajan et al.[32] and Suzuki et al..[33] (right) Variation of the effective electrical conductivity of the CL, σ_e^{eff}, as a function of the carbon + Pt volume fraction, ε_{c+Pt} (Eq. 33), along with the experimental data of Morris et al.[30] and Du et al.[31]

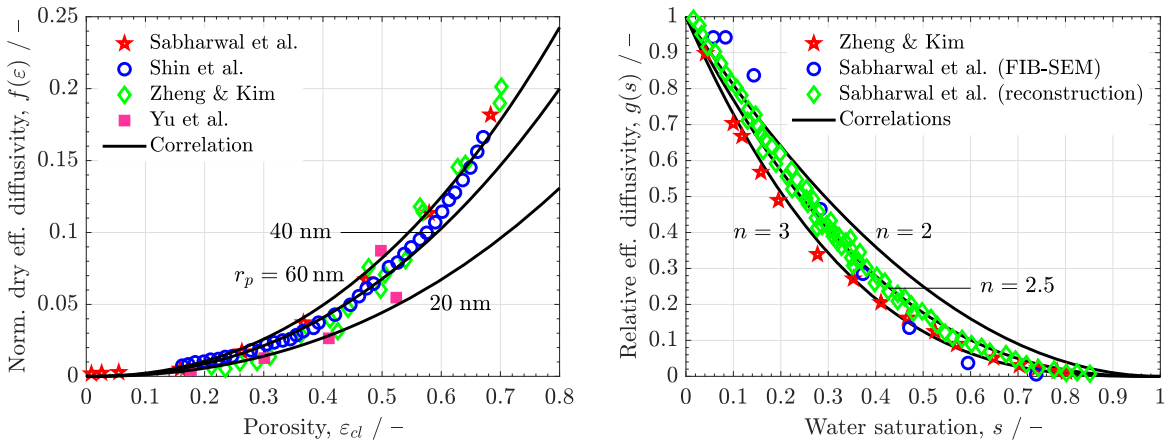

Figure 5. (Left) Normalized dry effective diffusivity, $f(\varepsilon) = D^{\text{eff,dry}}_{\text{O2,air}} / D^{\text{molec}}_{\text{O2,air}}$, as a function of the average porosity of the CL, ε_{cl}. The experimental and numerical data reported in previous works are included, together with the results corresponding to different pore radii, r_p (see Eqs. 6 and 34). (right) Relative effective diffusivity, $g(s) = D^{\text{eff,wet}}_{\text{O2,air}} / D^{\text{eff, dry}}_{\text{O2,air}}$, as a function of average saturation, s^{avg}. The numerical data reported in previous works are included, together with the results using different saturation exponents, n (see Eq. 36). All data are evaluated at $T = 80$ °C and $p_g = 1$ atm.

other numerical methods in order to avoid negative oxygen concentrations, thus improving the convergence and stability. The initial interval used in the algorithm was $C^{\text{Pt}}_{\text{O}_2} \in [0, C_{\text{O}_2}]$, setting $f(C^{\text{Pt}}_{\text{O}_2}) \leqslant 10^{-4}$ as the stop criterion. In addition, the *pdepe* solver was placed inside an outer iterative loop to satisfy the integral boundary conditions that depend on I^{avg} by using another bisection method expressed in terms of I^{avg}. In this case, the initial interval was set to $I^{\text{avg}} \in [0, I^{\text{avg}}_{\text{lim,chcl}}]$, where $I^{\text{avg}}_{\text{lim,chcl}} = 4FC^{in}_{\text{O}_2,ch} / R_{\text{O}_2,\text{chcl}}$ is the limiting current density associated with $R_{\text{O}_2,\text{chcl}}$. The stop criterion was set to an absolute variation lower than $\Delta I^{\text{avg}} \leqslant 10^{-5}$ A cm^{-2} between two consecutive iterations.

For a given V_{cell}, the average computational time of the serial implementation was around 10 s using a fine mesh with 50 elements. This resulted in approximately 3 min for the calculation of a full polarization curve from $V_{\text{cell}} = 1$ V to $V_{\text{cell}} = 0.2$ V in increments of $\Delta V_{\text{cell}} = 0.05$ V using a desktop laptop with Intel i7–7820HQ processors at 2.9 GHz and 16.0 GB of RAM.

Effective Transport Properties and Physicochemical Parameters

Typical values of parameters assumed constant based on previous experimental and numerical works are listed in Table I. Effective transport properties and electrochemical properties of interest that depend on the composition of the CL are discussed below, namely, ionic and electrical conductivity ($\sigma^{\text{eff}}_{\text{H}^+}$, $\sigma^{\text{eff}}_{e^-}$), mass diffusivity ($f(\varepsilon_{cl})$, $g(s^{\text{avg}})$), oxygen permeability coefficient (Ψ) and local transport coefficients (k_i), and ECSA and exchange current density (a_{ECSA}, $i_{o,c}$).

Figure 4 shows the correlations used for the effective ionic and electrical conductivities as a function of the volume fraction of the conductive phases, together with previously reported experimental data.[30–33,79] According to the works of Sabarirajan et al.,[32] Suzuki et al.[33] and Liu et al.,[79] the effective ionic conductivity at full humidification can be correlated as a function of the ionomer volume fraction, ε_e, by the following piecewise function

$$\sigma^{\text{eff}}_{\text{H}^+} = \begin{cases} 4.6\left(\dfrac{\varepsilon_e}{0.325}\right)^n & \varepsilon_e \leqslant 0.325 \\ 4.6 & \varepsilon_e > 0.325 \end{cases} \quad [\text{S m}^{-1}] \qquad [32]$$

For $0 \leqslant \varepsilon_e \leqslant 0.325$, the ionic conductivity increases with ε_e following a power law with an exponent $n \approx 2$. However, for larger values of ε_e, the ionic conductivity does not further increase because a larger amount of ionomer is accompanied by a growth of the tortuosity factor of the ionomer network (i.e., $\tau = \varepsilon_e / \sigma^{\text{eff}}_{\text{H}^+}$ increases).[32]

The electrical conductivity (at high relative humidity) can be approximately correlated as a function of the volume fraction of carbon and Pt, $\varepsilon_{c+\text{Pt}}$, through a linear function[30,31]

$$\sigma^{\text{eff}}_{e^-} = 1.5 \times 10^3(\varepsilon_{c+\text{Pt}} - 0.1) \quad [\text{S m}^{-1}] \qquad [33]$$

A percolation threshold exists for $\varepsilon_{c+\text{Pt}} \approx 0.1$ due to poor interconnection of carbon particles caused by ionomer and water.

Comparatively, the ionic conductivity is around two orders of magnitude lower than the electrical conductivity for similar volume fractions of the conductive phase. Moreover, the CL ionic conductivity is around 10 times lower ($\sigma^{\text{eff}}_{\text{H}^+} \approx 0.05$–$5$ S m^{-1}) than that of the bulk membrane ($\sigma_{\text{H}^+,\text{pem}} \approx 10$ S m^{-1}) under well humidified conditions. In contrast, the electrical conductivity of the CL is comparable to that of the MPL and some carbon-paper GDLs.[29–31,80] Hence, large ohmic losses caused by proton transport usually warrant careful attention in CL design.

Regarding mass diffusivity, ε_{cl}/τ can be decomposed into the effect of the macro- and micro-scale porous structure of the CL based on the work of Inoue and Kawase[24]

$$\frac{\varepsilon_{cl}}{\tau} = \varepsilon^{2.2}_{\text{micro}} (1 - \Phi^{\text{iso}}_{\text{macro}})^{1.5} \qquad [34]$$

where $\varepsilon_{\text{micro}}$ is the apparent micro-porosity and $\Phi^{\text{iso}}_{\text{macro}}$ is the volume fraction of isolated macropores, which do not contribute to gas diffusion. As discussed in Ref. 24 $\Phi^{\text{iso}}_{\text{macro}}$ can be estimated from the normalized cumulative pore volume distribution of the CL, typically representing around a 20% of the porosity (i.e., $\Phi^{\text{iso}}_{\text{macro}} \approx 0.2\varepsilon_{cl}$). $\varepsilon_{\text{micro}}$ can be determined using ε_{cl} and $\Phi^{\text{iso}}_{\text{macro}}$ as follows

$$\varepsilon_{cl} = (1 - \Phi^{\text{iso}}_{\text{macro}})\varepsilon_{\text{micro}} + \Phi^{\text{iso}}_{\text{macro}} \Rightarrow$$
$$\varepsilon_{\text{micro}} = \frac{\varepsilon_{cl} - \Phi^{\text{iso}}_{\text{macro}}}{1 - \Phi^{\text{iso}}_{\text{macro}}} \qquad [35]$$

The variation of $f(\varepsilon_{cl})$ is shown in Fig. 5, along with experimental and numerical data extracted from various literature sources.[20–23] For an intermediate pore radius, $r_p = 40$ μm, $f(\varepsilon_{cl})$ varies around 40% when the porosity is varied by 0.1 ($\Delta\varepsilon_{cl} = 0.1$). Whereas for an intermediate porosity, $\varepsilon_{cl} = 0.5$, $f(\varepsilon_{cl})$ varies around 24% when the

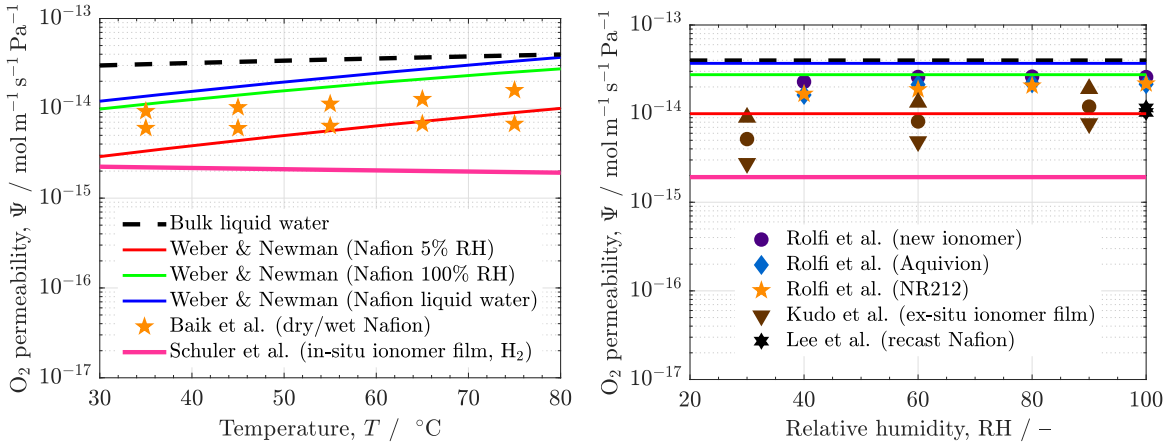

Figure 6. Variation of the oxygen permeability coefficient, Ψ, with (left) temperature, T, and (right) relative humidity, RH, corresponding to bulk liquid water (independent of RH),[73] and experimental data reported for dry/wet membranes and ionomer films from ex situ and in situ experiments.[81,83–85,92]

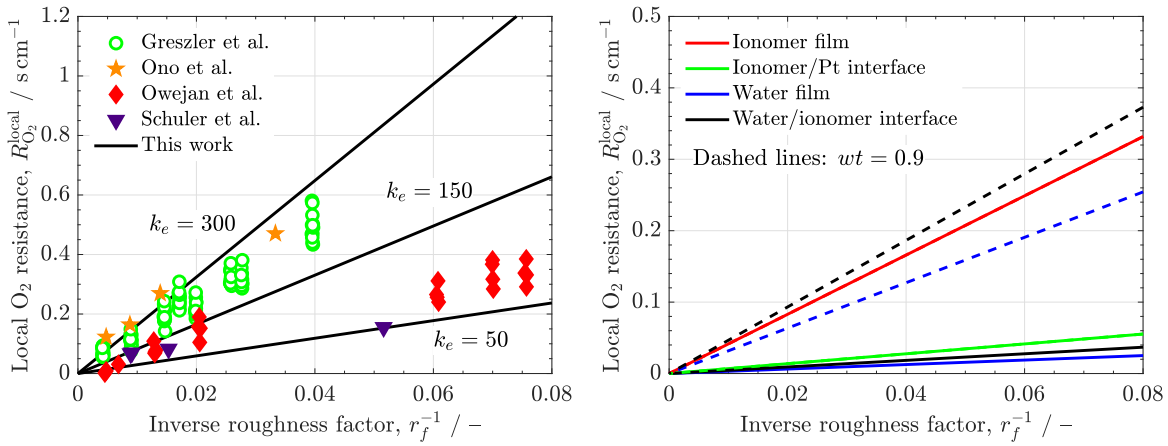

Figure 7. (Left) Variation of the local oxygen transport resistance, $R_{O_2}^{local}$, as a function of the inverse of the roughness factor, r_f^{-1}, for different values of k_e (50, 150, 300), compared to previous experimental data.[54,57,93,94] (right) Break-down of the contributions of the ionomer and water films and their interfaces to the local oxygen transport resistance for two different Pt/C weight ratios, $wt = 0.5$ (solid lines) and $wt = 0.9$ (dashed lines), corresponding to $k_e = 10^2$. $k_w = 4$, $k_{we} = 1/6$ and $k_{Pt} = 1/6$.

pore radius is varied by 20 μm ($\Delta r_p = 20$ μm). Therefore, the influence of both variables on $f(\varepsilon_{cl})$ cannot be neglected, although the impact of porosity is somewhat larger.

The relative effective diffusivity, $g(s^{avg})$, can be modeled as a power law according to previous numerical works[20,22]

$$g(s^{avg}) = (1 - s^{avg})^n \quad [36]$$

where the saturation exponent is $n \approx 2.5$.

As commented before , given the variability expected in the local oxygen transport resistances of water, ionomer and Pt interface, it is convenient to express these resistances in terms of a well established reference. A good choice is the permeability coefficient of oxygen in bulk liquid water, Ψ_w, which depends on temperature through the following expression[73]

$$\Psi_w = \Psi_w^{ref} \exp\left[\frac{E_w}{R}\left(\frac{1}{303.15} - \frac{1}{T}\right)\right] \quad [37]$$

where E_w is the activation energy of oxygen permeation (see Table I).

According to previous works, the local transport coefficient in water can be reasonably assumed to be $k_w \sim 1$ in order to account for the effect of non-equilibirum dissolution of oxygen in thin water films.[60,64,81,82] However, the transport coefficients associated with the ionomer film and its interfaces, k_{we}, k_e and k_{Pt}, deserve further attention. Recent experimental data of Schuler et al.[56,57] have shown that the diffusive resistance in the ionomer film is usually dominant, and the interfacial resistances only sum up to one-third of the ionomer resistance. According to these results, it can be concluded that $k_{we} \sim k_{Pt} \sim 10^{-1}$. As shown in Fig. 6, the permeability coefficient of oxygen in thin ionomer films measured in situ ($\delta_e \sim 1-10$ nm)[56,57] is around one order of magnitude lower than that reported before for membranes[81,83–85] and ionomer films from ex situ experiments ($\delta_e \approx 20-100$ nm)[81] (i.e., around two orders of magnitude lower than Ψ_w). The low oxygen permeability in CL ionomer films can be explained by finite-size interactions,[86,87] which result in the formation of a dense ionomer region near the Pt interface. This barrier must be ascribed to the ionomer film rather than to interfacial adsorption kinetics (i.e., the effective diffusivity across the ionomer film is not constant).[81,88–91] Additionally, the heterogeneous microstructure of ionomer and morphological changes arising from the ionomer deposition compared to conventional film casting methods in ex situ experiments can contribute to explain the lower values found in CLs.[56,57] As a result, k_e is expected to be in the range $k_e \sim$ 10–100 in most situations.

In terms of the formulation, it is worth noting that the transport resistances associated to k_w and k_{we} play a similar role, since they are proportional to the surface area of active ionomer (i.e., ionomer covering platinized carbon particles). In contrast, the transport resistances associated to k_e and k_{Pt} are proportional to the active

area of Pt (including the effect of the extended diffusion length across the ionomer). This circumstance is shown in Fig. 7, which shows the predicted local oxygen transport resistance for different values of $k_e = 50 - 300$ compared to previous experimental data,[54,57,93,94] together with the break-down of the contributions of water, ionomer and interfacial resistances (k_w, k_{we} and k_{Pt} are fixed equal to 4 (~ 1), 1/6 ($\sim 10^{-1}$) and 1/6 ($\sim 10^{-1}$), respectively.[56,57]) For a given CL composition (and operating conditions), from Eq. 24 can be seen that the local oxygen transport resistance increases linearly with the inverse of the roughness factor, $r_f^{-1} = A_{geo}/A_{Pt,cl}^{active} = (a_{ECSA} L_{Pt})^{-1}$, i.e.,

$$R_{O_2}^{local} = \left[\frac{A_{film+w}}{A_{film}} R_w + R_{we} + \frac{A_{film}}{A_{Pt}^{active}}(R_e + R_{Pt})\right]\frac{A_{geo}}{A_{e,cl}} \quad [38a]$$

$$= \left[\Gamma R_w + R_{we} + \frac{A_{film} x n_c n_{Pt}}{A_{Pt}^{active} x n_c n_{Pt}}(R_e + R_{Pt})\right]\frac{A_{geo}}{A_{e,cl}} \quad [38b]$$

$$= \left[\frac{A_{Pt,cl}^{active}}{A_{e,cl}}(\Gamma R_w + R_{we}) + \frac{1}{1-\theta_{PtO}}(R_e + R_{Pt})\right]\underbrace{\frac{A_{geo}}{A_{Pt,cl}^{active}}}_{r_f^{-1}} \quad [38c]$$

where $A_{geo}/A_{e,cl} = (\delta_{cl} a_e x)^{-1}$ is the ratio between the geometric area and the total surface area of active ionomer, x is the volume fraction of Pt-loaded carbon particles, n_c is the volume fraction of carbon particles, and n_{Pt} is the number of active Pt nano-particles on a Pt/C particle. Thus, $x n_c n_{Pt}$ is equal to the number of Pt particles per unit CL volume.

As shown in Fig. 7, the model and the experimental data are in good agreement in the expected range of variation of $k_e \sim 10 - 10^2$. According to Eq. 38c, the slope of the oxygen transport resistance of the ionomer and the ionomer/Pt interface are independent of wt (and x). In other words, for a given geometric area, both resistances increase with decreasing area of active Pt (lower L_{Pt} and/or a_{ECSA}). However, the slope of the local transport resistances of the water film and the water/ionomer interface are sensitive to wt due to its dependency on the area ratio $A_{Pt,cl}^{active}/A_{e,cl}$. This ratio can be expressed as

$$\frac{A_{Pt,cl}^{active}}{A_{e,cl}} = \frac{1}{\delta_{cl} a_e x} = \frac{r_f \rho_c r_c^3}{3 L_{Pt}(r_c + \delta_e)^2}\left(\frac{wt}{1-wt}\right)$$
$$= \Upsilon \rho_c r_c \left(\frac{wt}{1-wt}\right) a_{ECSA} \quad [39]$$

where the factor $wt(1-wt)^{-1}$ is equal to

$$L_{Pt} = x\frac{\delta_{cl}}{f_t}\left(\frac{wt}{1-wt}\right) \Rightarrow \frac{wt}{1-wt} = \frac{L_{Pt}}{\rho_c}\frac{1}{\delta_{cl} x \varepsilon_c} \quad [40]$$

Considering the above two equations, it can be seen that for a given Pt loading (and ρ_c, r_c, δ_e and a_{ECSA}), $A_{Pt,cl}^{active}/A_{e,cl}$ increases for decreasing δ_{cl}, x and ε_c (i.e., higher $wt(1-wt)^{-1}$). Consequently, when the thickness is fixed (δ_{cl} = const.), $A_{Pt,cl}^{active}/A_{e,cl}$ increases with lower x and/or ε_c. Alternatively, when all carbon particles area platinized ($x = 1$), $A_{Pt,cl}^{active}/A_{e,cl}$ increases with lower δ_{cl} and/or ε_c. In physical terms, this means that for a given Pt loading, the overall oxygen flux (current density) demanded over the geometric area is distributed among a lower number of water films and water/ionomer interfaces, so that there is an increase of the local oxygen flux toward each active Pt site (at a given current density). This is reflected by an increase of the local oxygen transport resistance per unit geometric area. In contrast, the diffusive resistance of the thin ionomer film is not affected by this aspect because the increase of the local oxygen flux due to a lower number of ionomer films (carbon particles) is offset by a decrease of the effective diffusion length through the ionomer film (i.e., it just depends on the active area of Pt, as commented before). In addition, the resistance at the ionomer/Pt interface is proportional in nature to the active area of Pt and inversely proportional to the roughness factor.

Quantitatively, the contribution of each transport resistance can be determined based on the slopes, s_i, of the graph $R_{O_2}^{local}$ vs r_f^{-1}. The relative fractions of each term, χ_i, are given by

$$R_{O_2,w}^{local} = \frac{A_{Pt,cl}^{active}}{A_{e,cl}} R_w^{eff} r_f^{-1} = \Upsilon \rho_c r_c \left(\frac{wt}{1-wt}\right) a_{ECSA} \Gamma R_w r_f^{-1} \Rightarrow$$
$$\chi_w = \frac{s_w}{s_w + s_{we} + s_e + s_{Pt}} \quad [41a]$$

$$R_{O_2,we}^{local} = \frac{A_{Pt,cl}^{active}}{A_{e,cl}} R_{we} r_f^{-1} = \Upsilon \rho_c r_c \left(\frac{wt}{1-wt}\right) a_{ECSA} R_{we} r_f^{-1} \Rightarrow$$
$$\chi_{we} = \frac{s_e}{s_w + s_{we} + s_e + s_{Pt}} \quad [41b]$$

$$R_{O_2,e}^{local} = R_e r_f^{-1} \Rightarrow \chi_e = \frac{s_{we}}{s_w + s_{we} + s_e + s_{Pt}} \quad [41c]$$

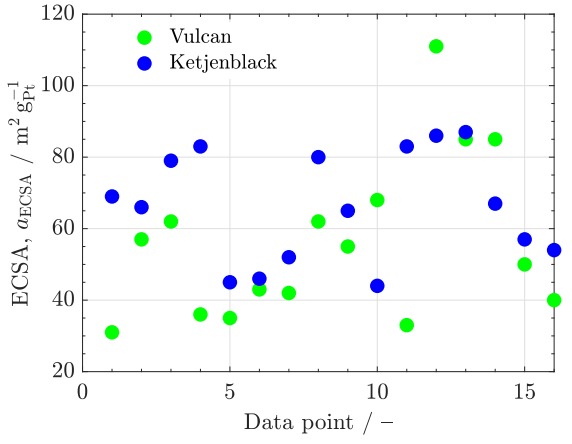

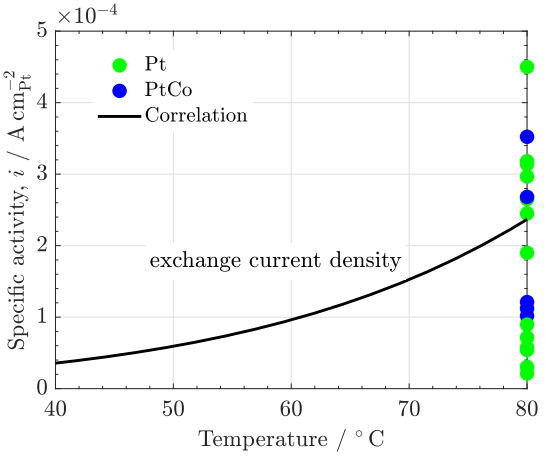

Figure 8. (Left) ECSA, a_{ECSA}, and (right) specific catalytic activity, i, reported by different authors for Pt and PtCo catalysts supported on Vulcan and Ketjenblack.[36–48] The average values are equal to $a_{ECSA}^{avg} \approx 60$ m^2 g$_{Pt}^{-1}$ and $i^{avg} \approx 2 \times 10^{-4}$ A cm$_{Pt}^{-2}$ ($T = 80$ °C). The correlation used in this work for the exchange current density as a function of temperature is shown on the right (see Eq. 13). Collected data were taken with pure oxygen at RH = 100% and p_g = 1–1.5 bar ($C_{O_2}^{ref,avg} \approx 40$ mol m^{-3}).

Table II. Operating conditions and transport and physicochemical parameters used in the validation campaign against the experimental data of Sun et al.[69] and Owejan et al.[55].

Parameter	Symbol	Value	References
Operating temperature	T	65 °C (Sun et al.)	69
		80 °C (Owejan et al.)	55
Operating pressure	$p_{g,a}$, $p_{g,c}$	1 bar (Sun et al.)	69
		1.5 bar (Owejan et al.)	55
Operating relative humidity	RH_a, RH_c	100%	55, 69
Channel-CL mass transport resistance	$R_{\mathrm{O_2,chcl}}$	1.1 s cm^{-1} (Sun et al.)	69
		0.7 s cm^{-1} (Owejan et al.)	55
Area-specific ionic resistance	$\mathrm{ASR}_{\mathrm{pem}}$	0 (Sun et al.)	69
		2.1×10^{-2} cm^2 S^{-1} (Owejan et al.)	11, 55
Ionomer-to-carbon weight ratio	I/C	0.7 (Sun et al.)	69
		0.95 (Owejan et al.)	55
Electrochemical surface area	a_{ECSA}	30, 21.5 m^2 $\mathrm{g}_{\mathrm{Pt}}^{-1}$ (Sun et al.)	69
		40−80 m^2 $\mathrm{g}_{\mathrm{Pt}}^{-1}$ (Owejan et al.)	55
Local O_2 transport coefficients	k_w, k_{we}, k_e, k_{Pt}	4, 1/6, 450, 1/6 (Sun et al.)	Estimated
		4, 1/6, 70, 1/6 (Owejan et al.)	

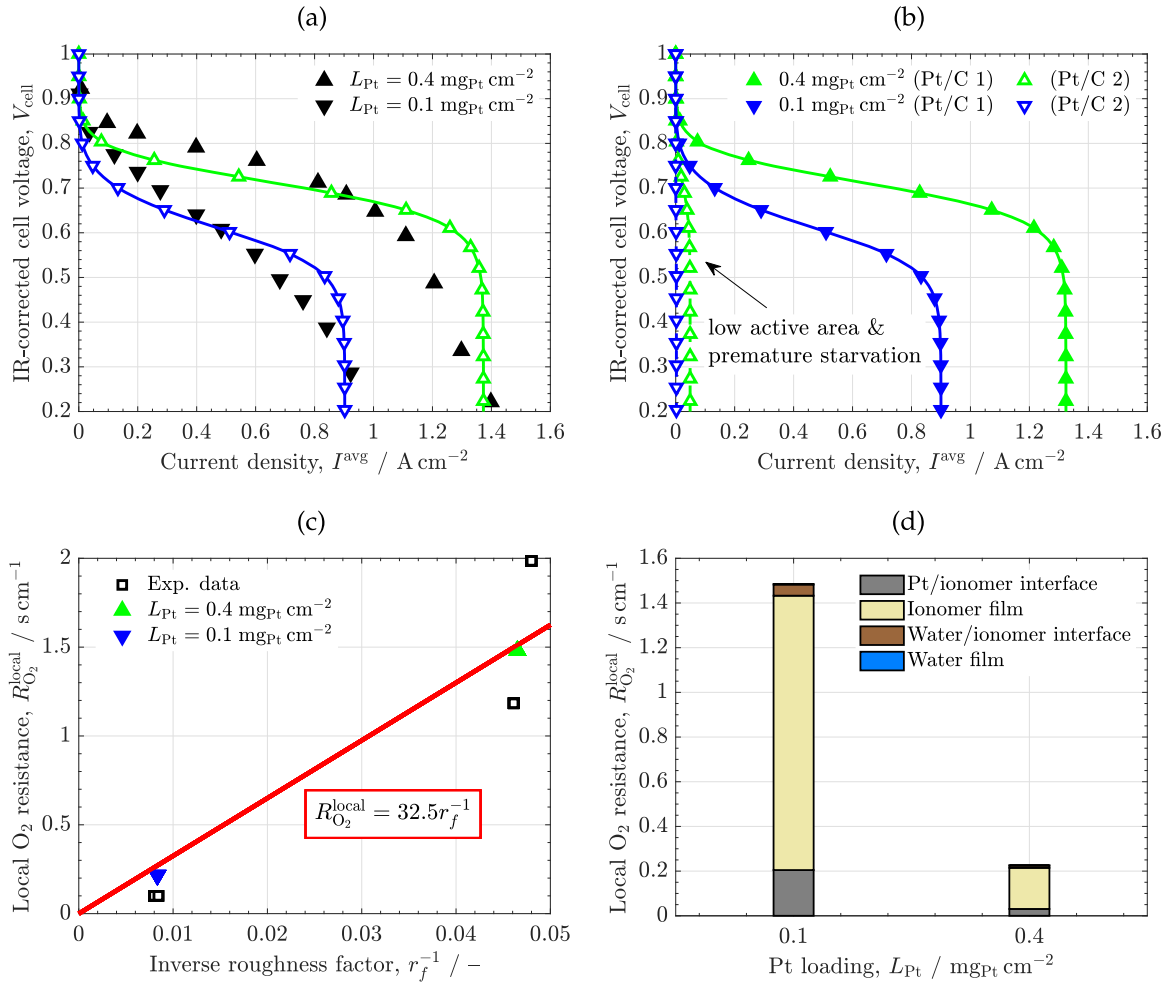

Figure 9. (a), (b) Comparison between the polarization curves predicted by the present model and the experimental data of Sun et al.[69] (black symbols), corresponding to two CLs with a Pt loading of $L_{\mathrm{Pt}} = 0.1$, 0.4 $\mathrm{mg_{Pt}}$ cm^{-2} and two Pt/C catalysts ($wt_1 = 0.5$, $wt_2 = 0.1$). The right plot shows the break-down of the polarization curves of each Pt/C catalyst computed with the present model. (c,d) Comparison between the local oxygen transport resistance, $R_{\mathrm{O_2}}^{\mathrm{local}}$, predicted by the present model and the experimental data of Sun et al.[69] (black symbols), as a function of the inverse of the roughness factor, r_f^{-1}. The linear fit to the numerical data is included. The right plot shows the break-down of $R_{\mathrm{O_2}}^{\mathrm{local}}$ of the Pt/C catalyst with the lowest local resistance (Pt/C 1).

$$R^{\text{local}}_{\text{O}_2,\,\text{Pt}} = R_{\text{Pt}} r_f^{-1} \Rightarrow \chi_{\text{Pt}} = \frac{s_{\text{Pt}}}{s_w + s_{we} + s_e + s_{\text{Pt}}} \qquad [41\text{d}]$$

For $wt = 0.5/0.9$, the resulting values are $\chi_w = 5.6/25.1\%$, $\chi_{we} = 8.2/36.8\%$, $\chi_e = 73.9/32.7\%$ and $\chi_{\text{Pt}} = 12.3/5.4\%$. The effect of $R^{\text{local}}_{\text{O}_2,e}$ is important in all situations, while $R^{\text{local}}_{\text{O}_2,w} \sim R^{\text{local}}_{\text{O}_2,we}$ becomes comparable to $R^{\text{local}}_{\text{O}_2,e}$ for $wt = 0.9$. $R^{\text{local}}_{\text{O}_2,Pt}$ represents a small amount between 5%–10%.

Regarding electrochemical properties, Fig. 8 shows the ECSA and specific catalytic activity collected from multiple literature sources for Pt and PtCo catalysts supported on Vulcan (low porosity and specific carbon surface area) and Ketjenblack (high porosity and specific carbon surface area). These two Pt/C catalysts were selected due to their extended use in industry and research. The data are randomly distributed among authors, and no clear trend can be observed depending on the support and/or catalyst type. The ECSA ranges between 30 $\text{m}^2\,\text{g}_{\text{Pt}}^{-1}$ and 110 $\text{m}^2\,\text{g}_{\text{Pt}}^{-1}$, being the differences between both carbon supports small, $a^{\text{avg}}_{\text{ECSA,V}} \approx 56\ \text{m}^2\,\text{g}_{\text{Pt}}^{-1}$ vs $a^{\text{avg}}_{\text{ECSA, KB}} \approx 66.4\ \text{m}^2\,\text{g}_{\text{Pt}}^{-1}$. The mean value of the full dataset is equal to $a^{\text{avg}}_{\text{ECSA}} \approx 61.2\ \text{m}^2\,\text{g}_{\text{Pt}}^{-1}$. Analyzing the specific activity, the data of both catalysts are almost the same, $i^{\text{avg}}_{\text{Pt}} \approx i^{\text{avg}}_{\text{PtCo}} \approx 2 \times 10^{-4}\ \text{A cm}^2_{\text{Pt}}$ at $T = 80\ ^\circ\text{C}$, $\text{RH} = 100\%$ for a reference oxygen concentration $C^{\text{ref}}_{\text{O}_2} \approx 40\ \text{mol m}^{-3}$. The similar activity of PtCo to Pt makes this alloy catalyst very attractive for reducing the Pt content in commercial applications, while preserving performance (e.g., Toyota Mirai[95]). The mean exchange current density agrees well with that predicted by Eq.13 at 80 °C, $i_{o,c} \approx 2.4 \times 10^{-4}\ \text{A cm}^2_{\text{Pt}}$.

Model Validation

In this section, the model predictions are compared against the experimental data of Sun et al.[69] and Owejan et al..[55] The dataset of Sun et al.[69] provides a reference case to validate the model in terms of $R^{\text{local}}_{\text{O}_2}$, considering fully platinized cathode CLs (i.e., $x = 1$) with two Pt/C catalysts ($L_{\text{Pt}} = 0.1,\ 0.4\ \text{mg}_{\text{Pt}}\,\text{cm}^{-2}$) and different thicknesses ($\delta_{cl} \neq$ const.), and similar volumetric composition, i.e., ε_{cl}, ε_e, ε_c, ε_{Pt}, $r_p \approx$ const. On the other hand, the dataset of Owejan et al.[55] provides a case to examine the effect of carbon dilution ($x < 1$) on cathode CLs with either one or two Pt/C catalysts ($L_{\text{Pt}} = 0.025 - 0.3\ \text{mg}_{\text{Pt}}\,\text{cm}^{-2}$), having a similar thickness and volumetric composition. In total, ten CLs were examined, two from the work of Sun et al.[69] with air feed and eight from the work of Owejan et al.[55] with both air and oxygen feed, under fully humidified conditions. The microstructural and compositional parameters

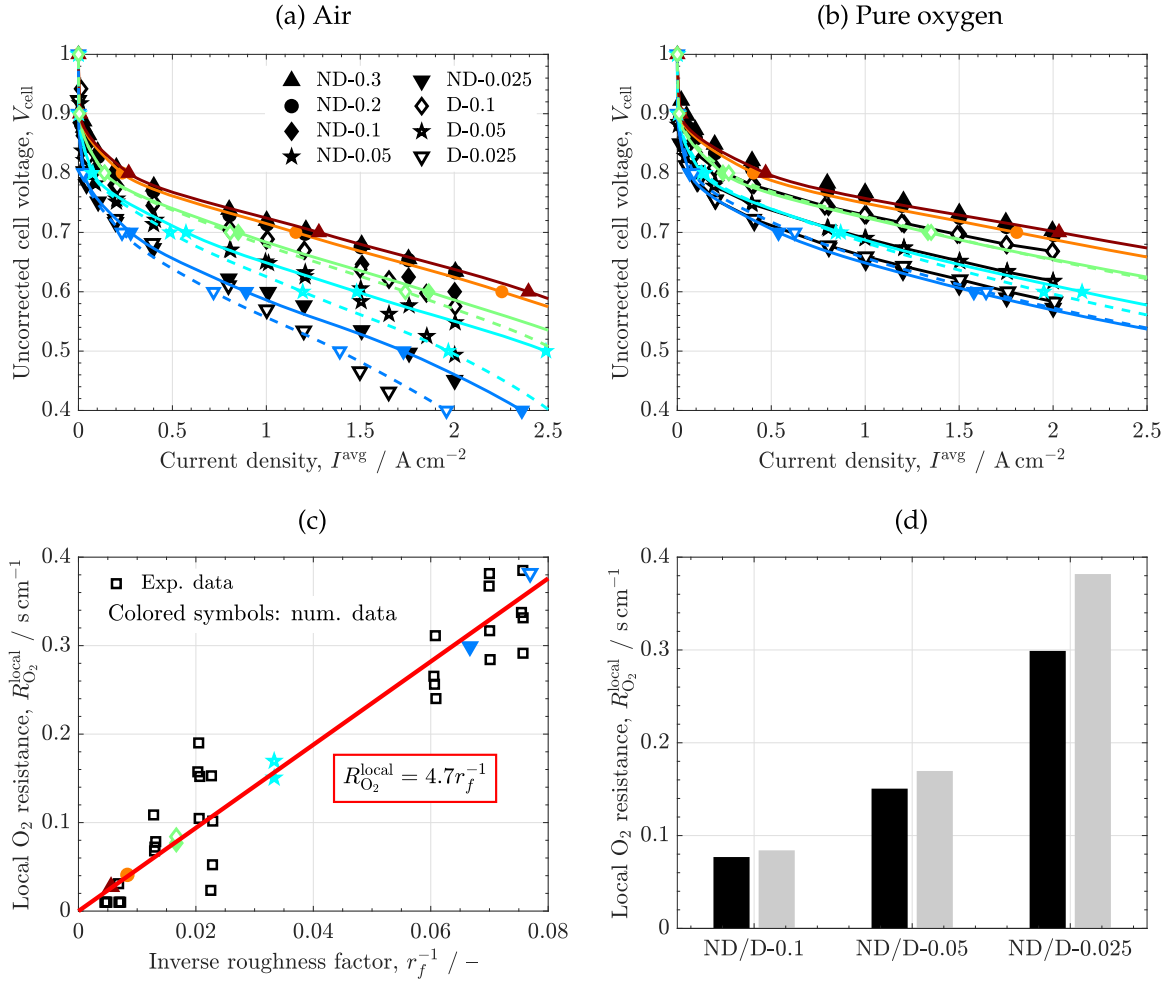

Figure 10. (a), (b) Comparison between the polarization curves predicted by the model and the experimental data of Owejan et al.[55] (black symbols), corresponding to CLs with a Pt loading in the range $L_{\text{Pt}} = 0.025{-}0.3\ \text{mg}_{\text{Pt}}\,\text{cm}^{-2}$ and either one or two Pt/C catalysts. The CL thickness is approximately constant, including both diluted (D) and non-diluted (ND) CLs with bare carbon. The results for air-fed and oxygen-fed PEFCs are included. (c), (d) Comparison between the local oxygen transport resistance, $R^{\text{local}}_{\text{O}_2}$, predicted by the present model and the experimental data of Owejan et al.[55] (black symbols). The right plot shows a comparison of the computed $R^{\text{local}}_{\text{O}_2}$ for diluted and non-diluted CL samples.

determined according to the properties reported in these works are provided in Supplementary Material (available online at stacks.iop.org/JES/168/124514/mmedia). The operating conditions and specific transport and physicochemical properties used in the validation campaign are listed in Table II.

Figure 9 shows the predicted IR-corrected polarization curves, together with the data of Sun et al.[69] for two CLs with $L_{Pt} = 0.1$ and $0.4\ mg_{Pt}\ cm^{-2}$, incorporating two Pt/C catalysts ($wt_1 = 0.5$, $x_1 = 0.76 - 0.98$; $wt_2 = 0.1$, $x_2 = 0.02 - 0.24$). The IR-corrected polarization curves computed for each Pt/C catalyst are also shown in the upper part. The model successfully reproduces the main features of the experimental data despite the formulation simplifications. According to Eqs. 22 and 24, the effect of a local reduction of $L_{Pt,i}$ is two-fold: (i) it lowers $a_{Pt,i}^{active}$, decreasing the current density for a given overpotential, η_c, and (ii) it increases $R_{O_2,i}^{local}$ (i.e., $r_{f,i}^{-1}$ increases), leading to premature oxygen starvation. The active specific surface areas and the local transport resistances vary between $a_{Pt,1}^{active} = 10.2/11.7\ \mu m^{-1}$–$a_{Pt,2}^{active} = 0.36/0.03\ \mu m^{-1}$ and $R_{O_2,1}^{local} = 0.23/6.1\ s\ cm^{-1}$–$R_{O_2,2}^{local} = 1.5/568.2\ s\ cm^{-1}$ for $L_{Pt} = 0.4/0.1\ mg_{Pt}\ cm^{-2}$, respectively. This result highlights the importance of preserving a high ECSA and avoiding local heterogeneities (e.g., variations of the ionomer film thickness) at low Pt loading to ensure an even distribution of the oxygen flux among active Pt sites.

The local oxygen transport resistance is compared with the data of Sun et al.[69] on the bottom part of Fig. 9. $R_{O_2}^{local}$ increases from around $0.25\ s\ cm^{-1}$ to $1.5\ s\ cm^{-1}$ in agreement with the increment of r_f^{-1} from 8×10^{-3} to 4.8×10^{-2} (a factor of six). The linear fit to the numerical results is given by $R_{O_2}^{local} = 32.5 r_f^{-1}$. For moderate wt values, the contribution of the local ionomer resistance, $R_{O_2,e}^{local}$, is dominant, representing around 80% of the total resistance. The impact of $R_{O_2}^{local} \sim R_{O_2,e}^{local}$ on performance is particularly strong in the case of Sun et al.[69] due to the high ionomer transport coefficient, $k_e = 450$, compared to other works in the literature ($k_e \approx 50 - 300$). As a result, the limiting current density at low Pt loading significantly decreases when the overall oxygen transport resistance experiences relative variations of order unity (i.e., $\Delta R_{O_2}^{local} \sim R_{O_2,chcl} + R_{O_2,cl}^{local}$).

The validation against the data of Owejan et al.[55] is shown in Fig. 10, including results for both air-fed and oxygen-fed PEFCs. The examined CLs include Pt loadings ranging between $L_{Pt} = 0.025 - 0.3\ mg_{Pt}\ cm^{-2}$ with either one or two Pt/C catalysts, which are diluted (D) and non-diluted (ND) with bare carbon to keep the thickness approximately constant ($\delta_{cl} \approx 12\ \mu m$). The effect of $R_{O_2}^{local}$ is significantly higher with air feed compared to pure oxygen feed owing to the five-fold lower oxygen concentration in air. This leads to a direct increase of the limiting current density and significantly better performance, especially at medium-to-low voltages ($V_{cell} \lesssim 0.7\ V$). As a reference, the power density achieved with pure oxygen at $V_{cell} \approx 0.7\ V$ for high Pt loading ($L_{Pt} = 0.3\ mg_{Pt}\ cm^{-2}$) is $P_{O_2} \approx 1.4\ W\ cm^{-2}$, which is around 30% higher compared to that with air feed, $P_{air} \approx 0.91\ W\ cm^{-2}$. The difference increases with decreasing Pt loading. For ultra-low Pt loading, $L_{Pt} = 0.025\ mg_{Pt}\ cm^{-2}$, the achieved power densities under the same conditions are $P_{O_2} = 0.42\ W\ cm^{-2}$ vs $P_{air} = 0.21\ W\ cm^{-2}$, representing a relative increment of 100%. For instance, the performance with air feed at $L_{Pt} = 0.025\ mg_{Pt}\ cm^{-2}$ drops significantly when $V_{cell} \lesssim 0.5\ V$ due to local mass transport limitations ($R_{O_2}^{local} \sim R_{O_2,chcl} \approx 0.3\ s\ cm^{-1}$), an effect that is not visible in the curves with oxygen feed. Comparing the results of the diluted and non-diluted samples, the addition of bare carbon has a negative impact on performance (being the effect larger for air feed and low Pt loadings). The performance drop is caused by an increase of $R_{O_2}^{local}$ due to: (i) a reduction of a_{ECSA} (see Table II) and (ii) an increment of wt (lower x), which increases $R_{O_2,w}^{local}$ and $R_{O_2,we}^{local}$. In addition, for a given Pt loading, CL dilution leads to thicker samples compared to non-diluted samples with the same wt and ε_c, thus increasing bulk mass transport and ionic transport losses.

The variation of $R_{O_2}^{local}$ with r_f^{-1} is shown on the bottom part of Fig. 10. The numerical and experimental results are in good agreement, even though the scatter observed in the experiments is somewhat larger. The linear dependency of $R_{O_2}^{local}$ with r_f^{-1}, $R_{O_2}^{local} = 4.7 r_f^{-1}$, is significantly lower than that found in the case of Sun et al.[69] because of the lower value of $k_e = 70$ (vs. $k_e = 450$). $R_{O_2,e}^{local}$ remains as the main contributor to $R_{O_2}^{local}$ despite the variations of $R_{O_2,w}^{local}$ and $R_{O_2,we}^{local}$ caused by carbon dilution. The differences between diluted and non-diluted samples increase non-linearly with Pt loading due to the non-linear variation of a_{ECSA}[55] and the inverse dependency of $R_{O_2,w}^{local}$ and $R_{O_2,we}^{local}$ on x, which takes the values $x = 0.26$, 0.12 and 0.05 for $L_{Pt} = 0.1$, 0.05 and $0.025\ mg_{Pt}\ cm^{-2}$, respectively.

Conclusions

A mathematical model for the cathode catalyst layer (CL) in polymer electrolyte fuel cells (PEFCs) has been presented. The model accounts for proton and electron conduction and oxygen diffusion across the CL using a 1D macroscopic formulation, which is locally coupled to a 1D microscopic model that describes local transport of oxygen from the bulk pore space toward active Pt sites through water and ionomer films and their interfaces. Both single and variably loaded Pt/C catalysts, diluted and non-diluted with bare carbon, have been considered in the analysis. The oxygen concentration drop from the channel to the CL inlet and the ionic potential drop across the membrane are incorporated through integral boundary conditions.

The model was complemented with experimental data from multiple literature sources to describe effective transport properties as a function of the volume fractions of carbon, ionomer, Pt and void volume (porosity), as well as local oxygen transport resistances and electrochemical properties, the electrochemical surface area (ECSA) and the exchange current density. The predictive capabilities of the model were validated against previous experimental data in terms of cell performance and local oxygen transport resistance, $R_{O_2}^{local}$. $R_{O_2}^{local}$ showed a linear dependency with the inverse of the roughness factor (i.e., the ratio between the geometric area and the active area of Pt), with a significant contribution of the resistance of the thin ionomer film regardless of the Pt/C weight ratio (wt). The resistances of the ionomer film and ionomer/Pt interface do not depend on wt due to the constant value of the roughness factor at a given Pt loading (if the ECSA is not affected by changes in wt and Pt loading). However, the contribution of the local resistances of the water film and water/ionomer interface depends on wt, being comparable to that of the ionomer at high wt values. This is caused by the decrease of the surface area of active ionomer (i.e., platinized carbon particles) per unit of geometric area at high wt, so that the overall oxygen flux is divided among a lower number of water films and water/ionomer interfaces. In addition, the results showed that for a given Pt loading, CLs that are non-diluted with bare carbon perform better than diluted samples. This is explained by the higher value of $R_{O_2}^{local}$ in diluted samples with similar thickness but higher wt.

In summary, an increase of the ECSA and the active ionomer area per unit of geometric area in non-diluted CLs is crucial to mitigate the adverse effect of $R_{O_2}^{local}$ at low Pt loading. Future work should focus on a parametric analysis to identify optimal CL composition and the impact of key parameters, such as the ECSA, exchange current density, average saturation and ionomer transport coefficient, at different Pt loadings. In addition, the effect of CL

heterogeneities on performance and durability should be examined, including two-phase water transport and non-isothermal effects.

Acknowledgments

This work was supported by the projects PID2019-106740RB-I00 and EIN2020-112247 (Spanish Agencia Estatal de Investigación) and the project PEM4ENERGY-CM-UC3M funded by the call "Programa de apoyo a la realización de proyectos interdisciplinares de I + D para jóvenes investigadores de la Universidad Carlos III de Madrid 2019–2020" under the frame of the "Convenio Plurianual Comunidad de Madrid-Universidad Carlos III de Madrid".

ORCID

Arturo Sánchez-Ramos https://orcid.org/0000-0002-1410-4500
Jeff T. Gostick https://orcid.org/0000-0001-7736-7124
Pablo A. García-Salaberri https://orcid.org/0000-0002-3918-5415

References

1. F. Barbir and T. Gomez, *International Journal of Hydrogen Energy*, **22**, 1027 (1997).
2. H. Lohse-Busch, K. Stutenberg, M. Duoba, and S. Iliev, *Technology Assessment of a Fuel Cell Vehicle: 2017 Toyota Mirai* (2018).
3. T. Teng, X. Zhang, H. Dong, and Q. Xue, *International Journal of Hydrogen Energy*, **45**, 20293 (2020).
4. C. Sealy, *Mater. Today*, **11**, 65 (2008).
5. P. Ferreira et al., *J. Electrochem. Soc.*, **152**, A2256 (2005).
6. X. Yu and S. Ye, *Journal of Power Sources*, **172**, 133 (2007).
7. A. Kongkanand and M. F. Mathias, *The Journal of Physical Chemistry Letters*, **7**, 1127 (2016).
8. A. Z. Weber and A. Kusoglu, *Journal of Materials Chemistry A*, **2**, 17207 (2014).
9. M. Breitwieser, M. Klingele, B. Britton, S. Holdcroft, R. Zengerle, and S. Thiele, *Electrochemistry Communications*, **60**, 168 (2015).
10. Y. V. Yakovlev, Y. V. Lobko, M. Vorokhta, J. Nováková, M. Mazur, I. Matolínová, and V. Matolín, *Journal of Power Sources*, **490**, 229531 (2021).
11. N. Ureña, M. T. Pérez-Prior, B. Levenfeld, and P. A. García-Salaberri, *Polymers*, **13**, 363 (2021).
12. K. Talukdar, S. Delgado, T. Lagarteira, P. Gazdzicki, and K. A. Friedrich, *Journal of Power Sources*, **427**, 309 (2019).
13. M. Folgado, J. Conde, P. Ferreira-Aparicio, and A. Chaparro, *Fuel Cells*, **18**, 602 (2018).
14. S. Holdcroft, *Chemistry of Materials*, **26**, 381 (2014).
15. J. J. Conde, M. A. Folgado, P. Ferreira-Aparicio, A. M. Chaparro, A. Chowdhury, A. Kusoglu, D. Cullen, and A. Z. Weber, *Journal of Power Sources*, **427**, 250 (2019).
16. G. S. Harzer, A. Orfanidi, H. El-Sayed, P. Madkikar, and H. A. Gasteiger, *J. Electrochem. Soc.*, **165**, F770 (2018).
17. V. Yarlagadda, M. K. Carpenter, T. E. Moylan, R. S. Kukreja, R. Koestner, W. Gu, L. Thompson, and A. Kongkanand, *ACS Energy Lett.*, **3**, 618 (2018).
18. A. Serov, A. D. Shum, X. Xiao, V. De Andrade, K. Artyushkova, I. V. Zenyuk, and P. Atanassov, *Applied Catalysis B: Environmental*, **237**, 1139 (2018).
19. Y. Kim, T. Asset, F. Wei, P. Atanassov, M. Secanell, J. Barralet, and J. Gostick, *Materials Today Energy*, **20**, 100641 (2021).
20. M. Sabharwal, L. M. Pant, N. Patel, and M. Secanell, *J. Electrochem. Soc.*, **166**, F3065 (2019).
21. S. Shin, A. R. Kim, and S. Um, *Electrochimica Acta*, **275**, 87–99 (2018).
22. W. Zheng and S. H. Kim, *J. Electrochem. Soc.*, **165**, F468 (2018).
23. Z. Yu, R. Carter, and J. Zhang, *Fuel Cells*, **12**, 557 (2012).
24. G. Inoue and M. Kawase, *Journal of Power Sources*, **327**, 1 (2016).
25. J. Zhao, S. Shahgaldi, I. Alaefour, Q. Xu, and X. Li, *Applied Energy*, **209**, 203 (2018).
26. O. S. Burheim, H. Su, H. H. Hauge, S. Pasupathi, and B. G. Pollet, *International Journal of Hydrogen Energy*, **39**, 9397 (2014).
27. R. Bock, H. Karoliussen, B. G. Pollet, M. Secanell, F. Seland, D. Stanier, and O. S. Burheim, *International Journal of Hydrogen Energy*, **45**, 1335 (2020).
28. M. Ahadi, M. Tam, M. S. Saha, J. Stumper, and M. Bahrami, *Journal of Power Sources*, **354**, 207 (2017).
29. M. Ahadi, J. Jankovic, M. Tam, B. Zahiri, M. Saha, J. Stumper, and M. Bahrami, *Fuel Cells*, **19**, 550 (2019).
30. D. R. Morris, S. P. Liu, D. Villegas Gonzalez, and J. T. Gostick, *ACS Applied Materials & Interfaces*, **6**, 18609 (2014).
31. C. Du, P. Shi, X. Cheng, and G. Yin, *Electrochemistry Communications*, **6**, 435 (2004).
32. D. C. Sabarirajan, J. Liu, Y. Qi, A. Perego, A. T. Haug, and I. V. Zenyuk, *J. Electrochem. Soc.*, **167**, 084521 (2020).
33. T. Suzuki, H. Murata, T. Hatanaka, and Y. Morimoto, *R&D Review of Toyota CRDL*, **39**, 33 (2003).
34. G. Li and P. G. Pickup, *J. Electrochem. Soc.*, **150**, C745 (2003).
35. R. Singh, A. Akhgar, P. Sui, K. Lange, and N. Djilali, *J. Electrochem. Soc.*, **161**, F415 (2014).
36. S. Zhang, X. Yuan, H. Wang, W. Mérida, H. Zhu, J. Shen, S. Wu, and J. Zhang, *International Journal of Hydrogen Energy*, **34**, 388 (2009).
37. J. Speder, A. Zana, I. Spanos, J. J. Kirkensgaard, K. Mortensen, M. Hanzlik, and M. Arenz, *Journal of Power Sources*, **261**, 14 (2014).
38. H. Yu, J. M. Roller, W. E. Mustain, and R. Maric, *Journal of Power Sources*, **283**, 84 (2015).
39. A. Chaparro, P. Ferreira-Aparicio, M. Folgado, E. Brightman, and G. Hinds, *Journal of Power Sources*, **325**, 609 (2016).
40. J. P. Braaten, S. Ogawa, V. Yarlagadda, A. Kongkanand, and S. Litster, *Journal of Power Sources*, **478**, 229049 (2020).
41. I. Gatto, A. Carbone, A. Saccà, E. Passalacqua, C. Oldani, L. Merlo, D. Sebastián, A. S. Aricò, and V. Baglio, *Journal of Electroanalytical Chemistry*, **842**, 59 (2019).
42. G. S. Harzer, A. Orfanidi, H. El-Sayed, P. Madkikar, and H. A. Gasteiger, *J. Electrochem. Soc.*, **165**, F770 (2018).
43. G. S. Harzer, J. N. Schwämmlein, A. M. Damjanović, S. Ghosh, and H. A. Gasteiger, *J. Electrochem. Soc.*, **165**, F3118 (2018).
44. M. Ko, E. Padgett, V. Yarlagadda, A. Kongkanand, and D. A. Muller, *J. Electrochem. Soc.*, **168**, 024512 (2021).
45. N. Macauley, D. D. Papadias, J. Fairweather, D. Spernjak, D. Langlois, R. Ahluwalia, K. L. More, R. Mukundan, and R. L. Borup, *J. Electrochem. Soc.*, **165**, F3148 (2018).
46. E. Padgett et al., *J. Electrochem. Soc.*, **166**, F198 (2019).
47. J. Speder, L. Altmann, M. Bäumer, J. J. Kirkensgaard, K. Mortensen, and M. Arenz, *RSC Adv.*, **4**, 14971 (2014).
48. H. Ungan and A. Bayrakçeken Yurtcan, *International Journal of Energy Research*, **43**, 5946 (2019).
49. S. J. Normile and I. V. Zenyuk, *Solid State Ionics*, **335**, 38 (2019).
50. P. Deevanhxay, T. Sasabe, S. Tsushima, and S. Hirai, *Electrochemistry communications*, **22**, 33 (2012).
51. T. Muzaffar, T. Kadyk, and M. Eikerling, *Sustainable Energy & Fuels*, **2**, 1189 (2018).
52. M. A. Sadeghi, J. Barralet, T. Friscic, and J. T. Gostick, *ECS Meeting Abstracts* (IOP Publishing) 1376 (2019).
53. S. Alam, E. Medici, K. Tajiri, and J. S. Allen, *ECS Trans.*, **92**, 29 (2019).
54. T. A. Greszler, D. Caulk, and P. Sinha, *J. Electrochem. Soc.*, **159**, F831 (2012).
55. J. P. Owejan, J. E. Owejan, and W. Gu, *J. Electrochem. Soc.*, **160**, F824 (2013).
56. F. B. Spingler, A. Phillips, T. Schuler, M. C. Tucker, and A. Z. Weber, *International Journal of Hydrogen Energy*, **42**, 13960 (2017).
57. T. Schuler, A. Chowdhury, A. T. Freiberg, B. Sneed, F. B. Spingler, M. C. Tucker, K. L. More, C. J. Radke, and A. Z. Weber, *J. Electrochem. Soc.*, **166**, F3020 (2019).
58. S. Salari, M. Tam, C. McCague, J. Stumper, and M. Bahrami, *Journal of Power Sources*, **449**, 227479 (2020).
59. W. Yoon and A. Z. Weber, *J. Electrochem. Soc.*, **158**, B1007 (2011).
60. L. Hao, K. Moriyama, W. Gu, and C. Y. Wang, *J. Electrochem. Soc.*, **162**, F854 (2015).
61. A. Goshtasbi, P. García-Salaberri, J. Chen, K. Talukdar, D. G. Sanchez, and T. Ersal, *J. Electrochem. Soc.*, **166**, F3154 (2019).
62. J. Liu, P. A. García-Salaberri, and I. V. Zenyuk, *Transport in Porous Media*, **128**, 363 (2019).
63. J. Liu, P. A. García-Salaberri, and I. V. Zenyuk, *J. Electrochem. Soc.*, **167**, 013524 (2019).
64. G. Gwak, J. Lee, M. Ghasemi, J. Choi, S. W. Lee, S. S. Jang, and H. Ju, *International Journal of Hydrogen Energy*, **45**, 13414 (2020).
65. Z. Zheng, F. Yang, C. Lin, F. Zhu, S. Shen, G. Wei, and J. Zhang, *Journal of Power Sources*, **451**, 227729 (2020).
66. P. García-Salaberri, D. Sánchez, P. Boillat, M. Vera, and K. A. Friedrich, *Journal of Power Sources*, **359**, 634 (2017).
67. P. García-Salaberri, *International Journal of Heat and Mass Transfer*, **167**, 120824 (2021).
68. D. Zapardiel and P. A. Garcia-Salaberri, *Journal of Power Sources*, **520**, 230735 (2021).
69. X. Sun, H. Yu, L. Zhou, X. Gao, Y. Zeng, D. Yao, L. He, and Z. Shao, *Electrochimica Acta*, **332**, 135474 (2020).
70. Q. Ye and T. Van Nguyen, *J. Electrochem. Soc.*, **154**, B1242 (2007).
71. T. Soboleva, X. Zhao, K. Malek, Z. Xie, T. Navessin, and S. Holdcroft, *ACS Applied Materials & Interfaces*, **2**, 375 (2010).
72. K. Jiao and X. Li, *Progress in Energy and Combustion Science*, **37**, 221 (2011).
73. R. H. P. Green and D. Perry's, "Physical and Chemical Data." *Chemical engineers' handbook* (McGraw-Hill, New York, NY) (1997).
74. I. V. Zenyuk, P. K. Das, and A. Z. Weber, *J. Electrochem. Soc.*, **163**, F691 (2016).
75. N. Subramanian, T. Greszler, J. Zhang, W. Gu, and R. Makharia, *J. Electrochem. Soc.*, **159**, B531 (2012).
76. B. Randrianarizafy, P. Schott, M. Gerard, and Y. Bultel, *Energies*, **13**, 2338 (2020).
77. Q. Meyer, I. Pivac, F. Barbir, and C. Zhao, *Journal of Power Sources*, **470**, 228285 (2020).
78. Y. T. Mu, A. Z. Weber, Z. L. Gu, T. Schuler, and W. Q. Tao, "Mesoscopic analyses of the impact of morphology and operating conditions on the transport resistances in a proton-exchange-membrane fuel-cell catalyst layer." *Sustainable Energy & Fuels*, **4**, 3623 (2020).
79. Y. Liu, M. W. Murphy, D. R. Baker, W. Gu, C. Ji, J. Jorne, and H. A. Gasteiger, *J. Electrochem. Soc.*, **156**, B970 (2009).
80. P. A. García-Salaberri, I. V. Zenyuk, A. D. Shum, G. Hwang, M. Vera, A. Z. Weber, and J. T. Gostick, *International Journal of Heat and Mass Transfer*, **127**, 687 (2018).

81. A. Z. Weber and J. Newman, *J. Electrochem. Soc.*, **151**, A311 (2004).
82. J. Liang, Y. Li, R. Wang, and J. Jiang, *Chemical Engineering Journal*, **400**, 125796 (2020).
83. K. D. Baik, B. K. Hong, and M. S. Kim, *International Journal of Hydrogen Energy*, **38**, 8927 (2013).
84. A. Rolfi, C. Oldani, L. Merlo, D. Facchi, and R. Ruffo, *Journal of Power Sources*, **396**, 95 (2018).
85. K. Lee, A. Ishihara, S. Mitsushima, N. Kamiya, and K. i. Ota, *J. Electrochem. Soc.*, **151**, A639 (2004).
86. A. Kusoglu, D. Kushner, D. K. Paul, K. Karan, M. A. Hickner, and A. Z. Weber, *Adv. Funct. Mater.*, **24**, 4763 (2014).
87. M. A. Modestino, A. Kusoglu, A. Hexemer, A. Z. Weber, and R. A. Segalman, *Macromolecules*, **45**, 4681 (2012).
88. R. Jinnouchi, K. Kudo, N. Kitano, and Y. Morimoto, *Electrochimica Acta*, **188**, 767 (2016).
89. Y. Kurihara, T. Mabuchi, and T. Tokumasu, *J. Electrochem. Soc.*, **164**, F628 (2017).
90. T. Mashio, H. Iden, A. Ohma, and T. Tokumasu, *Journal of Electroanalytical Chemistry*, **790**, 27 (2017).
91. Y. Kurihara, T. Mabuchi, and T. Tokumasu, *Journal of Power Sources*, **414**, 263 (2019).
92. K. Kudo, R. Jinnouchi, and Y. Morimoto, *Electrochimica Acta*, **209**, 682 (2016).
93. Y. Ono, T. Mashio, S. Takaichi, A. Ohma, H. Kanesaka, and K. Shinohara, *ECS Trans.*, **28**, 69 (2010).
94. J. P. Owejan, T. A. Trabold, and M. M. Mench, *International Journal of Heat and Mass Transfer*, **71**, 585 (2014).
95. A. Haug, "Novel ionomers and electrode structures for improved PEMFC electrode performance at low PGM loadings." *Annual Merit Review and Evaluation Meeting, DOE Hydrogen and Fuel Cells Program, Washington, DC* (2018).